J. Fluid Mech. (1984), *vol.* 138, *pp.* 93–127
Printed in Great Britain

Experimental investigation of jets in a crossflow

By J. ANDREOPOULOS AND W. RODI
Sonderforschungsbereich 80, University of Karlsruhe, Karlsruhe, F.R. Germany

(Received 10 November 1982 and in revised form 1 May 1983)

The paper reports on measurements in the flow generated by a jet issuing from a circular outlet in a wall into a cross-stream along this wall. For the jet-to-crossflow velocity ratios R of 0.5, 1 and 2, the mean and fluctuating velocity components were measured with a three-sensor hot-wire probe. The hot-wire signals were evaluated to yield the three mean-velocity components, the turbulent kinetic energy, the three turbulent shear stresses and, in the case of $R = 0.5$, the terms in the turbulent-kinetic-energy equation. The results give a quantitative picture of the complex three-dimensional mean flow and turbulence field, and the various phenomena as well as their dependence on the velocity ratio R are discussed in detail.

1. Introduction

Jets in a crossflow are of great practical relevance in a variety of engineering applications. Depending on the ratio R of jet to cross-stream velocity, examples of this flow can be found in turbomachinery (film cooling of turbine blades, jets into combustors), V/STOL aircraft in transition flight, and waste disposal into water bodies and the atmosphere. Because of the great practical significance, numerous experimental and theoretical studies have been carried out on the jet-in-a-crossflow problem. Some of the basic features associated with larger R-values as motivated by the V/STOL applications have been investigated experimentally by Keffer & Baines (1963), Komotani & Greber (1973) and Moussa, Trischka & Eskinazi (1977). Ramsey & Goldstein (1971) and Bergeles, Gosman & Launder (1976) reported measurements of the film-cooling effectiveness of the jets. The latter authors also measured velocity distributions and discovered that, for low velocity ratios R, the velocity profile across the exit plane of the jet can be considerably non-uniform. A more complete survey on mean-flow measurements can be found in Crabb, Durão & Whitelaw (1981). Very few measurements of turbulence quantities have been reported so far. Although it is established that, at high velocity ratios, the near field of jets in a crossflow is controlled largely by complex inviscid dynamics so that the influence of turbulence on the flow development is rather limited, the flow further downstream is always influenced by turbulence, and at small velocity ratios even the near field is turbulence-dominated. Hence turbulence measurements are important to complete the picture, and their absence hampers considerably the development of calculation methods, since a realistic modelling of the turbulent stresses and heat or mass fluxes requires an understanding of the turbulence processes, especially in the complex situation of a jet in a crossflow. The only turbulence measurements that included the shear stresses and not only the turbulent intensities were reported by Crabb *et al.* (1981) for the velocity ratios $R = 1.15$ and 2.3. Unfortunately, the accuracy of these turbulence measurements is somewhat doubtful because the profile of the shear stress $\overline{uw}$ shows a maximum at the plane of symmetry where $\overline{uw}$ should be zero. For low

velocity ratios (say $R = 0.5$), where the flow development is quite different from that at higher velocity ratios and turbulence effects are particularly important, no detailed turbulence measurements are available, and for all velocity ratios the measurements are not so detailed as to allow the deduction of the turbulent-kinetic-energy balance and hence an insight into the turbulence production, destruction and transport processes.

The objective of the research programme on which this paper partly reports was to increase understanding of the mean flow and turbulence characteristics of jets in a cross-stream at various velocity ratios and to obtain reliable and comprehensive turbulence data which can be used for testing and improving turbulence models. The experimental programme included a flow-visualization study, wall-static-pressure measurements, mean and fluctuating velocity measurements with hot-wire anemometers including the flow regions inside the discharge pipe, and concentration measurements. The results of the flow-visualization study in a water flume with point-dye injection and the investigation of the surface streaking patterns in a wind tunnel are reported in Foss (1980). The measurements inside the discharge pipe extended as far as three pipe diameters upstream of the exit and have shown clearly that, at low velocity ratios, the flow inside the pipe is influenced considerably by the cross-stream. These measurements are presented in Andreopoulos (1982). The present paper reports the measurements of mean and fluctuating velocities in the jet-in-a-cross-stream interaction region for the three velocity ratios $R = 0.5$, 1 and 2. The results of the concentration measurements are reported in Andreopoulos (*1983c*), while those on the pressure measurements will be presented in a future paper.

Section 2 discusses in some detail the general flow characteristics of jets in a crossflow. The experimental set-up and measurement techniques are described in §3. The results are presented and discussed in §4, and the paper ends with conclusions and recommendations for further work in §5.

2. General flow characteristics

The complicated nature of the jet in a crossflow is illustrated in figures 1 (*a*, *b*), where composite pictures of the flow development are presented for the velocity ratios $R = 0.5$ and 2 respectively. The flow behaviour shown in these figures was conceived from the flow-visualization measurements of Foss (1980) and from the present velocity measurements.

The most obvious feature of the jet in a crossflow is the mutual deflection of jet and crossflow. The jet is bent over by the cross-stream, while the latter is deflected as if it were blocked by a rigid obstacle, the difference being that the jet interacts with the deflected flow and entrains fluid from it. In the case of the small velocity ratio ($R = 0.5$), the flow behaves as if a partial, inclined 'cover' were put over the front part of the exit hole, causing the jet streamlines to start bending while still in the discharge tube and the jet to bend over completely right above the exit and also to lift up the oncoming flow over the bent-over jet. In the case of the higher velocity ratio ($R = 2$) the jet is only weakly affected near the exit and penetrates into the cross-stream before it is bent over. In both cases, wake regions with very complex three-dimensional flow patterns form in the lee of the jet. In these regions, the longitudinal velocity accelerates and the conservation of mass requires fluid to move from the sides towards the plane of symmetry. Very close to the wall a reverse-flow region forms, and cross-stream fluid has been observed to enter this region, travel upstream and then to be lifted upwards by the jet fluid and to be carried downstream

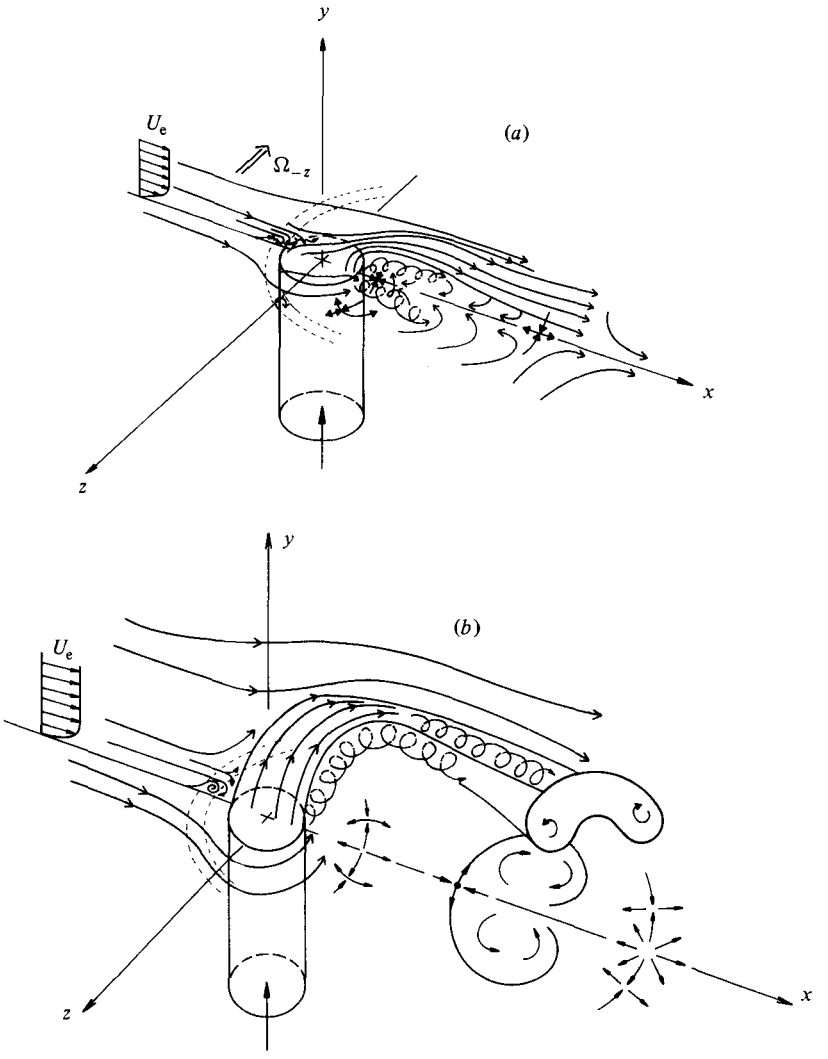

FIGURE 1. Flow development for (*a*) low ($R = 0.5$) and (*b*) high ($R = 2.0$) velocity ratios. Wall streak-lines according to Foss (1980).

together with it. Unlike the flow in two-dimensional situations, the flow does not recirculate in this highly three-dimensional case. Here the reverse flow is restricted to a region very near the wall. The surface streaking patterns given by Foss, which are time-integrated pictures of the flow, give a good indication of the extent of the reverse-flow zone.

The vorticity characteristics of a jet in a crossflow will now be discussed. An important feature of this flow is the deflection of the streamlines in the x- and z-directions and the associated reorientation and generation of vorticity. Particularly striking is the presence of streamwise vorticity downstream of the exit, which is contained in the secondary motion formed by two counterrotating vortices and gives the bent-over jet a kidney shape. This secondary motion decays in the downstream direction under the action of the turbulent stresses. We now consider how the vorticity of the approach flow is altered by the complex flow field ensuing from the

interaction of the jet in a cross-flow and how new vorticity is generated at the interface between the jet and the cross-stream. The approaching cross-stream boundary layer has negative Ω_z vorticity, while in the approaching pipe flow the vortex lines form concentric rings with the maximum vorticity near the pipe wall. On the sides, counterrotating Ω_x vorticity is therefore present in the tube flow. The oncoming negative Ω_z vorticity in the boundary layer is stretched by $\partial W/\partial z$ as the cross-stream is deflected around the jet, and the vorticity is thereby increased. The vortex lines are then bent around the jet and form a horseshoe vortex similar to that found when a boundary layer is deflected around an obstacle, for example by a cylinder mounted on a flat plate. Streamwise vorticity Ω_x is thereby formed, which is positive on the positive-z side of the symmetry plane and negative on the negative-z side of this plane. The oncoming boundary layer separates upstream of the jet as indicated in figures 1 (a, b). The surface streaking patterns obtained by Foss (1980) indicate that, for velocity ratios above $R = 0.6$, the flow between the separation point (first saddle point of the friction lines in these pictures) and the jet exit is rather complex.

According to Moussa *et al.* (1977), the mean vorticity issuing from the pipe is reoriented and bundles up into a pair of vortices that are bound to the lee surface of the jet. This formation of a bound vortex arises mainly owing to the different translation of different parts of the original ring vortex lines, and the two counter-rotating vortices can be thought to join at infinity. The resulting longitudinal vorticity is opposite to that of the horseshoe vortex. Moussa *et al.* ignored, however, a second mechanism, namely that vorticity generated at the interface of the initially orthogonal jet and cross-flow streams contributes also to the streamwise vorticity (see Foss 1980). First, Ω_x vorticity is directly generated at the interface and is increased by a stretching in the longitudinal direction. This generation arises from the large values of the normal velocity gradient in the z-direction, $\partial V/\partial z$, near the interface at the sides of the jet giving *positive* Ω_x for $z > 0$ and *negative* Ω_x for $z < 0$. Secondly, the interfacial shear also generates Ω_y vorticity, forming a vortex sheet around the jet which rolls up into two Ω_y concentrations aft of the jet, of opposite sign and on opposite sides of the centreplane. Part of this Ω_y vorticity is periodically shed, particularly at high R (see McMahen, Hester & Palfery, 1971); the remainder is bent over into the x-direction and strengthens the bound vortex. The generation of vorticity due to interfacial shear is important only at larger velocity ratios (say $R > 0.6$), while at small velocity ratios the bound streamwise vorticity stems mainly from the vorticity in the approaching tube flow. The bound vortex and the shed vorticity which dissolves into turbulence cause most of the entrainment of cross-stream fluid into the wake region and into the deflected jet. The bound vortex is much stronger than the horseshoe vortex having opposite vorticity, and there is some evidence given by Foss that the horseshoe vortex is swept into a 'hollow' of the kidney-shaped jet field underneath the bound vortex.

3. Experimental set-up and measurement techniques

The measurements were carried out in the closed-circuit wind tunnel of the Institut für Hydromechanik, University of Karlsruhe, which has an octagonally shaped working section 6 m long and 1.5 m in diameter. The characteristics of this wind tunnel are described in Ermshaus & Naudascher (1977). The experimental set-up is illustrated in figure 2. A flat plate was installed 0.28 m above the floor of the tunnel and the jet discharge was placed 10 exit diameters downstream from the leading edge

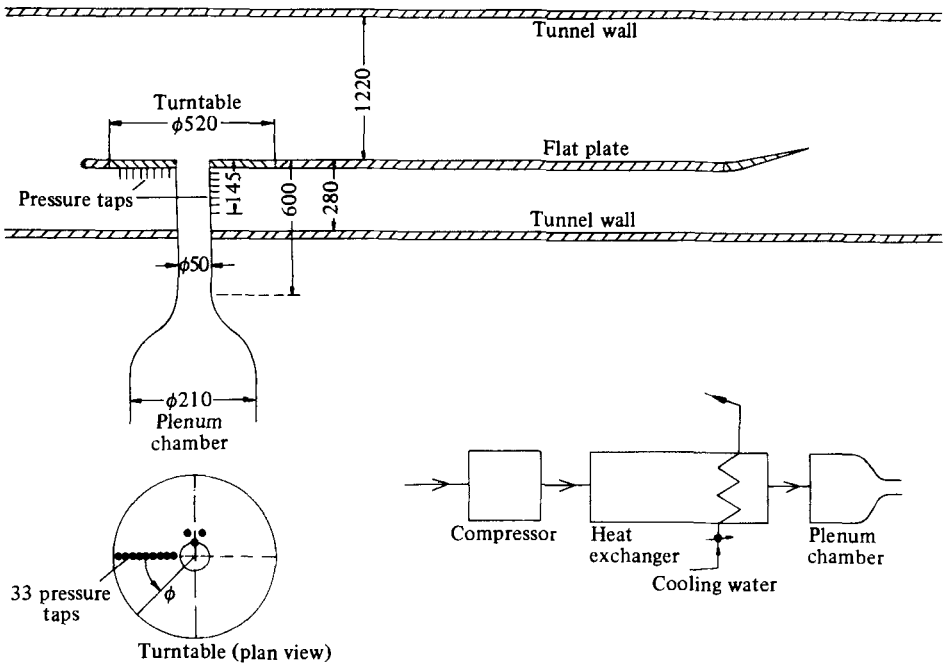

FIGURE 2. Experimental arrangement (dimensions in mm).

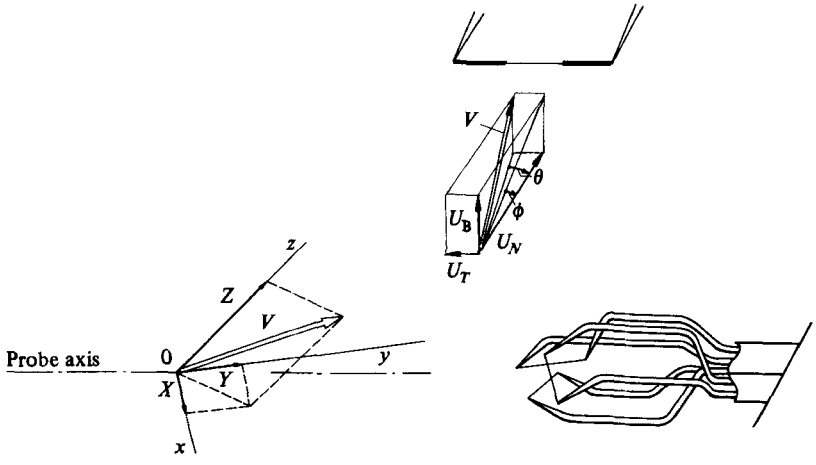

FIGURE 3. Triple-wire probe, probe coordinates and the relative pitch and yaw angles.

of the plate. The jet exited from a brass pipe of 50 mm internal diameter, the exit plane of the pipe being 12 diameters downstream of the plenum chamber, which was fed by a two-stage compressor, the temperature of the jet being controlled with the aid of a heat exchanger. The mean and turbulent velocity components were measured with DISA anemometers and DISA hot-wire probes. Miniature slant wire, cross-wire and triple-wire probes were successively used during the investigation. With the slant and cross-wire probes, only a limited number of turbulence quantities can be measured since the instantaneous values of the velocity vector cannot be obtained with these probes. On the other hand, these values can be extracted from the signals

of the triple-wire probe. All turbulence quantities reported here have been obtained with a triple hot-wire probe DISA Type 55P 91. The signals were fed into the analog-to-digital converter of the Hewlett-Packard Fourier Analyser 5451 C, digitized at 5 kHz per channel and stored on magnetic tape for later evaluation of the statistical averages. The data-acquisition system and the statistical analysis program are described in detail in Andreopoulos (1980). The probe was calibrated *in situ* and on-line with the aid of the computer, which makes the result independent of any possible attenuation or amplification in the process of transmitting signals from the anemometers to the computer or in the low-pass filters.

The triple-wire probe is illustrated in figure 3. The 3 wires are orthogonal to each other and parallel to the axes of the Cartesian coordinate system (x, y, z) as shown in figure 3. If the instantaneous velocity has the components X, Y, Z parallel to the respective axes x, y, z in the probe coordinates, then the effective cooling velocity for each wire is given by the following relations:

$$\left.\begin{aligned} U_{\mathrm{eff}1}^2 &= Y^2 + k_1^2(\phi_1)\,X^2 + h_1^2(\theta_1)\,Z^2, \quad \phi_1 = \tan^{-1}\frac{X}{Y}, \quad \theta_1 = \tan^{-1}\frac{Z}{Y}, \\ U_{\mathrm{eff}3}^2 &= X^2 + k_3^2(\phi_3)\,Z^2 + h_3^2(\theta_3)\,Y^2, \quad \phi_2 = \tan^{-1}\frac{Y}{Z}, \quad \theta_2 = \tan^{-1}\frac{X}{Z}, \\ U_{\mathrm{eff}2}^2 &= Z^2 + k_2^2(\phi_2)\,Y^2 + h_2^2(\theta_2)\,X^2, \quad \phi_3 = \tan^{-1}\frac{Z}{X}, \quad \theta_3 = \tan^{-1}\frac{Y}{X}, \end{aligned}\right\} \tag{1}$$

where k and h are coefficients for tangential and binormal cooling velocity components which have been obtained from individual calibrations of the wires. The above system of equations is linear with respect to the three unknowns X^2, Y^2, Z^2, and these instantaneous velocity components in probe coordinates can therefore be obtained easily by the matrix-inversion method. A similar technique has been described by Yavuzkurt, Moffat & Kays (1977), who inverted the matrix using a flow-analyser device whose analog output was digitized to give the velocity components. The present approach is fully digital (no linearizers were used) and has the novelty of allowing the coefficients k and h to vary with the pitch and yaw angles ϕ and θ defined in figure 3. These variations were determined directly by the calibrations. Since the yaw and pitch angles of the instantaneous velocity vector are not known *a priori*, an iterative numerical scheme has been used to solve the above equations. This method of accounting for the dependence of the k and h coefficients on the yaw and pitch angle has been first applied in the experiment described by Andreopoulos & Wood (1982), has been tested and documented by Andreopoulos (1981*a*, 1983*a*), and has been found to improve significantly the accuracy of the measurement technique, especially under situations of high turbulence intensities. This improvement is not surprising in view of the large amount of information put in from calibrations; the price to be paid for this is the somewhat increased computing time. Usually, the iterative scheme converges very rapidly (two iterations are enough) because the guessed starting value in the algorithm is the true value of the last digitized point. The iterations increase the computing time by about 25%. Typically, for one experimental point with 102400 digitized samples, about $3\frac{1}{2}$ min are required on average on a UNIVAC 1108 computer for data processing and storing the results for later plotting by CALOMP routines. Although the present method does not require previous knowledge of the mean velocity direction, the probe has been aligned parallel to the mean-flow direction in order to increase the accuracy of the measurements at high turbulence levels. Therefore two traverses had to be made in the measurement

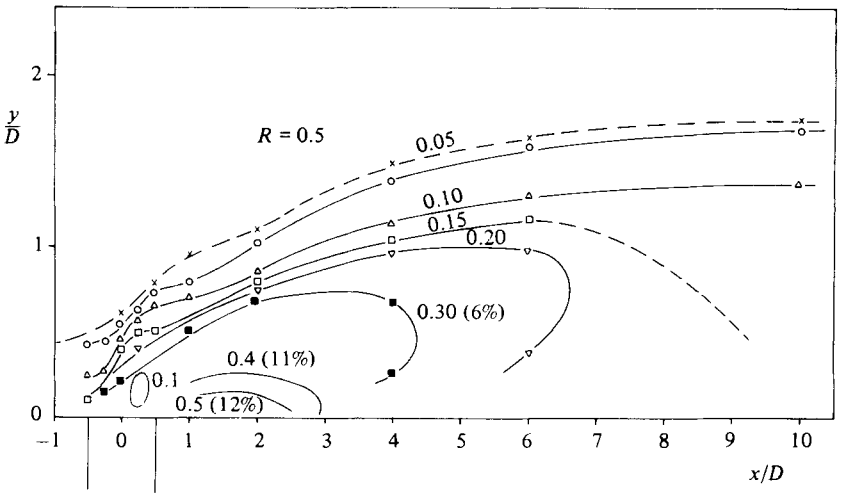

FIGURE 4. Contours of turbulence intensity $(\overline{u^2})^{\frac{1}{2}}/U$, with estimated measurement error in parentheses.

procedure: one traverse to find the mean-velocity vector and the second one to measure all Reynolds-stress components and higher-order moments. In the first traverse, the mean-velocity vector could be recovered quite accurately if the stem of the probe was within a cone with an apex semi-angle of 30° around the velocity vector. This has been demonstrated by a statistical error analysis for triple-wire probes (see Andreopoulos 1983*b*) and by the experimental results of Yavuzkurt *et al.* (1977). The reliability of the mean-velocity measurements has also been checked with the aid of the continuity equation. The mean-velocity gradients $\partial U/\partial x$, $\partial V/\partial y$ and $\partial W/\partial z$ have been obtained by graphical differentiation and were found to satisfy the continuity equation $\partial U_i/\partial x_i = 0$ within the accuracy limits of this differentiation.

The traverse gear on which the probe was mounted was driven by three step motors allowing a positioning of the probe with an accuracy of 0.025 mm in the y- and z-directions and 0.1 mm in the longitudinal direction (x). Hot-wire measurements inside the reverse-flow region close to the wall have not been attempted. However, since occasional flow reversals can take place also at larger distances from the wall, a tuft study has been undertaken in order to explore the regions in which instantaneous flow reversals may occur. In addition, the statistical error-analysis study (Andreopoulos 1983*b*) allows the error that must be expected in measurements with a triple wire to be related to the local turbulence intensity. Figure 4 shows measured contours of the turbulence intensity and the corresponding errors according to that study for the centreplane of the jet with a velocity ratio $R = 0.5$. At 30 % local turbulence intensity, an error of 6 % is to be expected. Results where the relative turbulence intensity is between 30 and 50 % have to be treated with caution because an error of up to 12 % is possible. Measurements in regions where the intensity is above 50 % are untrustworthy. Results will be presented in this paper only for regions where the turbulence intensity was below 35 %. It should be pointed out in this connection that hot-wire measurements in highly turbulent flows tend to overestimate the mean-flow velocities and underestimate the turbulence quantities.

The oncoming flat-plate boundary layer was tripped by means of a 1 cm wide sandpaper strip ten diameters upstream of the jet exit (that is, near the leading edge).

The pipe flow was also tripped by means of a small circumferential notch at the end of the contraction. Both oncoming flows were found to be developing turbulent flows for all the velocity ratios investigated. At $x/D = -4$ upstream of the jet exit, where the influence of the jet on the cross-stream boundary layer is still negligible, a friction coefficient of $c_f = 0.0037$ and a boundary-layer thickness of $\delta = 0.278D$ were measured at a cross-stream velocity $U_e = 13.9$ m/s. The freestream turbulence level at that velocity was 0.05%. The velocity ratios $R = 0.5$, 1 and 2 have been obtained by varying the jet exit velocity V_j, keeping the cross-stream velocity U_e constant. The corresponding Reynolds numbers based on the jet velocity and pipe diameter are 20500, 41000 and 82000 for the three velocity ratios respectively. These Reynolds numbers are roughly one order of magnitude higher than those in the flow-visualization studies of Foss (1980) performed in a flume, where both the approaching cross- and pipe flows were laminar. On the other hand, Foss obtained his surface-streaking pictures in the facility used for the present study and under comparable Reynolds numbers, but did not trip the boundary layer. However, it was found later by Foss (private communication) that the surface-streaking picture, qualitatively, was independent of Reynolds-number effects and/or of boundary-layer tripping.

4. Results and discussion

4.1. *Mean velocities*

Only a selection of the measured mean-velocity profiles at various downstream positions can be presented here for the three velocity ratios; further profiles will be available in a departmental report. Figures 5–7 show how the longitudinal mean velocity U varies with distance y from the wall at various downstream positions x. Figure 5 gives the profiles for the velocity ratio $R = 0.5$ at $z/D = 0$ and $z/D = -0.5$. The first 5 profiles correspond to x-positions above the exit and indicate a deceleration of the streamwise velocity while the last 5 profiles correspond to stations downstream of the exit and indicate accelerating flow in the wake region. For the position $x/D = 2$, the data of Bergeles *et al.* (1976) are included for comparison. The agreement with the present measurements can be seen to be quite good, even though these authors used a single wire to measure U, a method that is not very accurate in general three-dimensional flows. That the single-wire measurements agree quite well with the present three-sensor measurements is due to the fact that at $x/D = 2$ the V-component is small (the component W is zero at the centreplane anyway) so that the flow is predominantly in the x-direction and the velocity U could be obtained quite satisfactorily with a single sensor.

At $x/D = 1$ and 2, the velocity profiles show clearly the wake behaviour of the flow in the lee of the jet. A shear-layer region with fairly strong velocity gradient connects up the wake region near the wall and the freestream region. Very near the wall, where measurements could not be carried out, a reverse-flow region is expected to prevail according to the surface-streaking pattern observed by Foss (1980). It may also be expected that the measured velocities closest to the wall are not very accurate because they are already in a region of high turbulence intensity (see figure 4) where instantaneous flow reversal occurs. Near the outer edge, the velocity overshoots somewhat the freestream value, a feature that is much more pronounced in the cases of the higher velocity ratios, for which the profiles are shown in figures 6 and 7. For the case with $R = 2$ the overshoot disappears before $x/D = 6$, for the intermediate case of $R = 1$ the profile overshoots only down to about $x/D = 5$, while for the smallest velocity ratio $R = 0.5$ the overshoot has already disappeared at $x/D = 4$. It may come somewhat as a surprise that in this case there exists an overshoot at

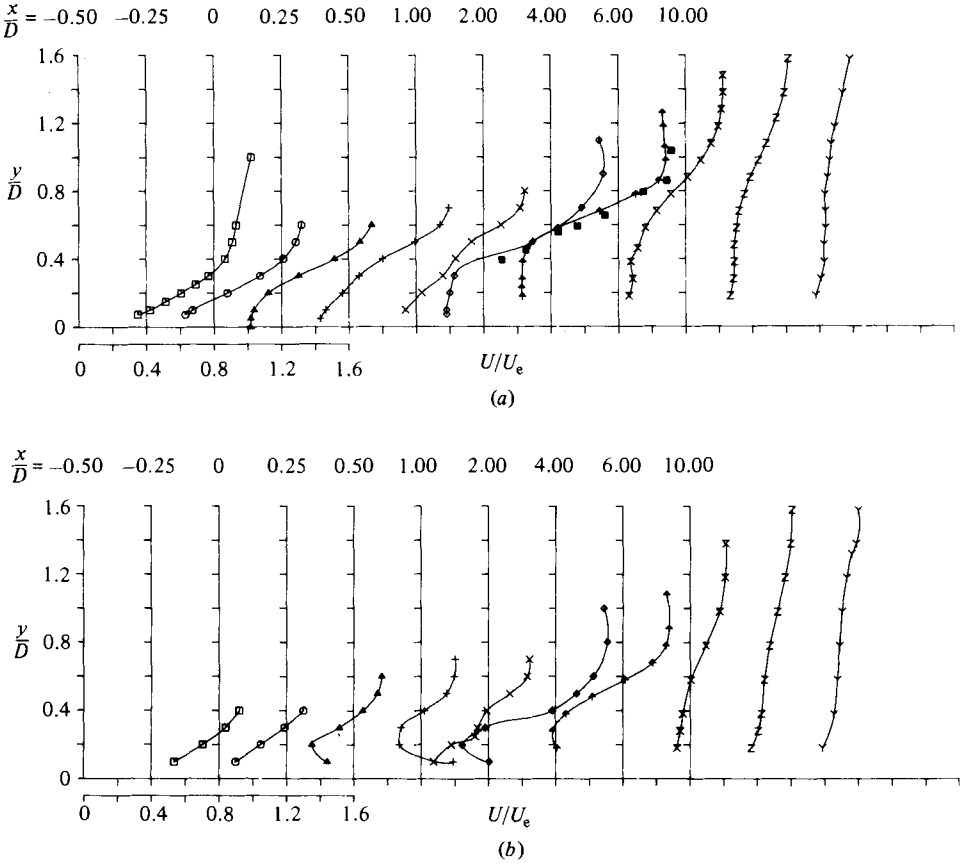

FIGURE 5. (*a*) Mean U-velocity profiles at the plane of symmetry $z/D = 0$ and $R = 0.5$: □, $x/D = -0.5$; ○, -0.25; △, 0.0; +, 0.25; ×, 0.50; ◇, 1.0; ⋔, 2.00; ⧖, 4; z, 6; Y, 10; ■, measurements of Bergeles *et al.* (1978). (*b*) Mean U-velocity profiles at $z/D = -0.5$; symbols as in (*a*).

all as the jet discharges with an average velocity only half the freestream velocity and an overshoot is thought to be due to the jet fluid having initially a velocity that is larger than the freestream velocity. However, as was explained in §2, the cross-stream fluid acts like a partial cover over the exit, causing the fluid to bend around and to accelerate so that the velocity of the bent-over jet is somewhat higher than the cross-stream velocity U_e. This becomes clear by looking at the streamline picture presented in figure 17 below.

The U-velocities at $z/D = -0.5$ are always higher than at the symmetry plane ($z = 0$) because the wake centre with low velocities is at the symmetry plane. Starting at $x/D = 0$, the velocity can even be seen to increase as the wall is approached. This behaviour is due to the deflection of the cross-stream around the jet near the wall, which causes an acceleration of the deflected flow.

At the higher velocity ratios $R = 1$ and 2, for which the U-velocity profiles are shown in figures 6 and 7 respectively, the jet penetrates further into the cross-stream, and the wake region in the lee of the jet is larger, associated also with a lower back pressure. This causes significant inflow towards the symmetry plane, which is enhanced near the wall also by the bound vortex motion and can be seen from the W-profiles in figures 11 and 13. This inward motion carries high-momentum fluid from the cross-stream to the symmetry plane and causes the maxima of U-velocity near

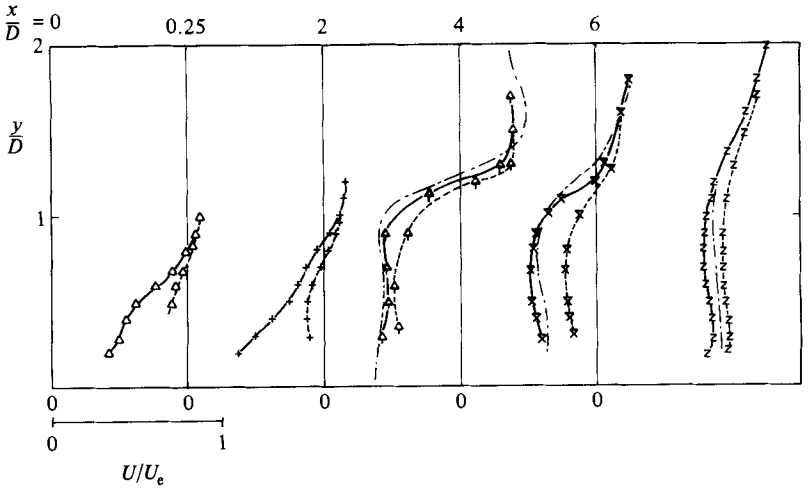

FIGURE 6. Mean U-velocity profiles for $R = 1$. Symbols as in figure 5. Solid lines $z/D = 0$; dotted lines $z/D = -0.5$; ———, mean line through the data of Ramsey & Goldstein (1971) at $x/D = 1.37$, 3.06 and 4.98 respectively.

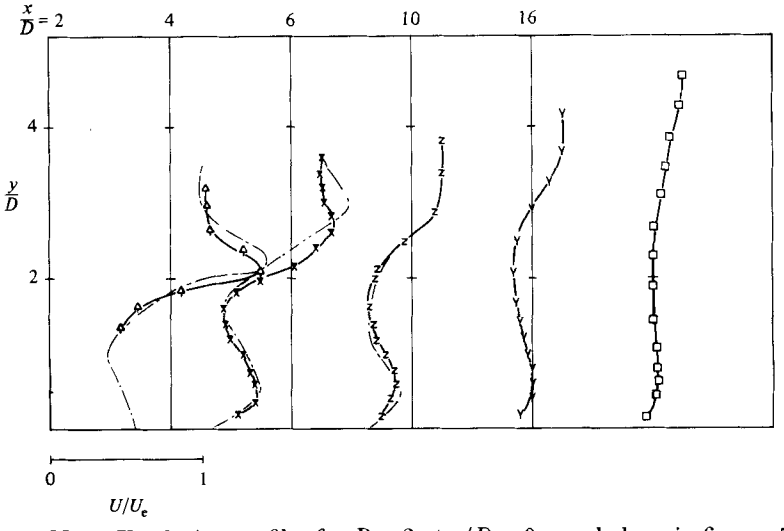

FIGURE 7. Mean U-velocity profiles for $R = 2$ at $z/D = 0$; symbols as in figures 5 and 6.

the wall that can be seen in figure 6 and 7. Non-monotonic velocity profiles develop, and the flow near the wall has wall-jet character. This development is strongest in the case of the largest velocity ratio ($R = 2$), and of course further downstream the velocity maximum near the wall disappears and the flow assumes boundary-layer character. In the intermediate range (for $R = 2$ at $x/D \approx 16$), where both wake and wall-jet regions have just disappeared, a fairly wide region having a low velocity gradient $\partial U/\partial y$ is set up which also has low turbulence production.

It then takes a while before the turbulence generated at the wall erodes this region and a normal boundary-layer profile is set up. Figure 6 compares directly the U-profiles at $z/D = 0$ and $z/D = -0.5$. Off the symmetry plane, U can be seen to be always higher than at $z = 0$ as the U-velocity is lowest at the centre of the wake region. The

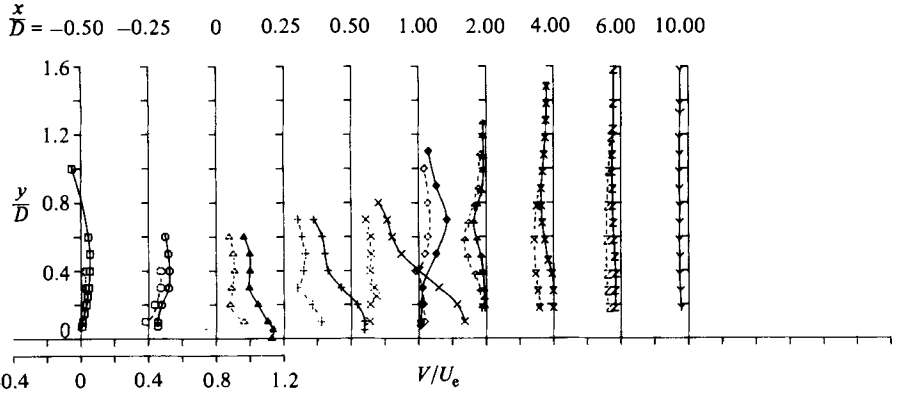

FIGURE 8. Mean V-velocity profiles for $R = 0.5$ at $z/D = 0$ (solid lines) and $z/D = -0.5$ (dotted line) respectively; symbols as in figure 5.

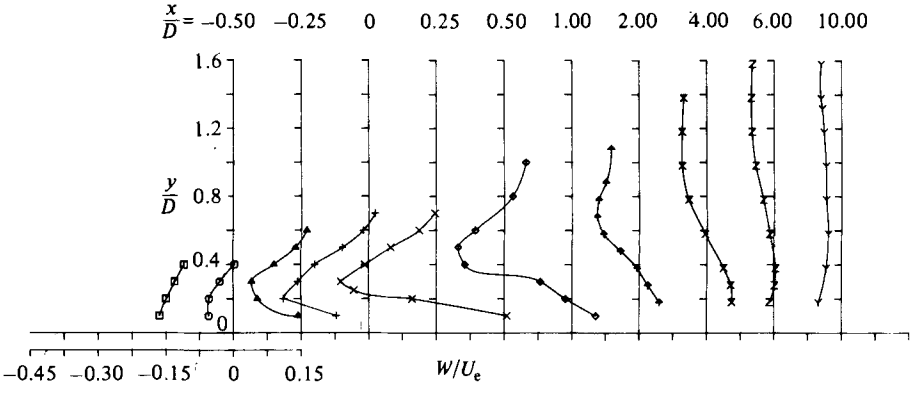

FIGURE 9. Mean W-velocity profiles for $R = 0.5$ at $z/D = -0.5$; symbols as in figure 5.

measurements indicate that the transverse velocity gradient $\partial U/\partial z$ has a monotonic behaviour. The data of Ramsey & Goldstein (1971) are included in figures 6 and 7 for comparison, even though they have been taken at somewhat different x-locations ($x/D = 1.37$, 3.06 and 4.58 instead of 2, 4 and 6). Bearing this in mind, the agreement must be considered fairly good.

In figures 8–16, measurements of the normal and transverse velocity components V and W are presented for the three velocity ratios. For $R = 0.5$, detailed measurements are given in the exit region. Figure 8 shows that, for this velocity ratio, the normal velocity V is small over the first quarter of the exit, but reaches values as high as $0.7U_e$ over the downstream part of the exit where the distribution is highly non-uniform. As has been already mentioned several times, the cross-stream acts like a partial cover over the exit and causes the flow inside the pipe to bend before reaching the exit and to leave the exit mainly near the downstream end. This cover effect has been shown to cause an acceleration so that the bent-over jet has a velocity which is somewhat higher than the freestream velocity. The bending over happens so quickly (see figure 17 below) that shortly downstream of the exit the normal velocity in the jet is nearly zero, as can be seen from the V-profile at $x/D = 1$. Of course, the jet lifts the cross-stream over it, and this causes the positive V-velocities at larger y-values shown in figure 8 at $x/D = 1$. Shortly after, however, the V-velocity changes

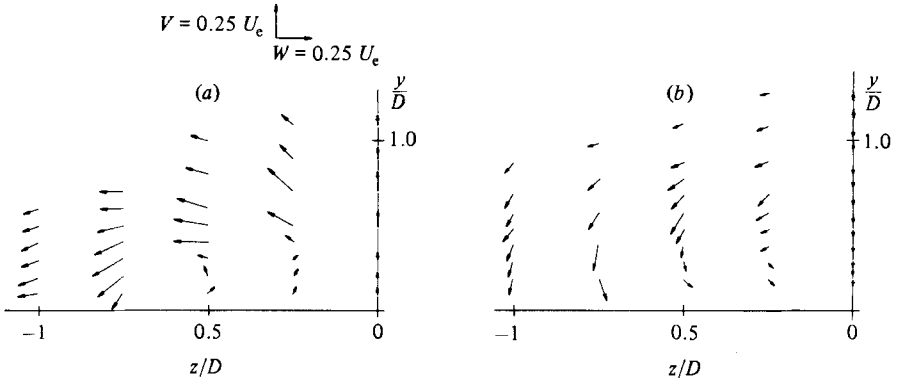

FIGURE 10. Secondary-motion velocity vectors for $R = 0.5$, at planes (*a*) $x/D = 1$ and (*b*) $x/D = 2$.

sign as the downwash effect of the wake region causes jet and cross-stream fluid to move towards the wall. Superimposed on this downward motion is a smaller upward motion due to the bound vortex in this region which can be seen clearly in figure 10. Apparently, however, the bound vortex decays rather quickly in this low-velocity-ratio case so that at $x/D = 6$ and 10 there is only a monotonic downward motion. The normal-velocity profiles off the symmetry plane show similar behaviour, but of course V is generally smaller than at $z = 0$, especially over the exit. The corresponding W-profiles at $z/D = -0.5$ are shown in figure 9; at the symmetry plane itself, the W-velocity is of course zero; the measurements indeed yielded only very small values. The reader is reminded that, in the coordinate system defined in figure 1, positive W-values at $z/D = -0.5$ represent an inward motion towards the symmetry plane and negative W-values an outward motion. The negative values in figure 9 near the exit are due to the deflection of the cross-stream around the jet near the wall. The induced outward motion is fairly strong as at $x/D = 0.5$ the lateral velocity reaches a maximum value of $0.35U_e$. Also, the lateral rate of strain $\partial W/\partial z$ is fairly large and reaches values of the order of $0.32U_e/D$ in front of the exit and hence causes significant stretching of the boundary-layer vorticity. Downstream of the exit, W changes sign near the wall as the low pressure in the wake region induces an inward flow. This inward flow near the wall and the outward flow further away are part of the bound vortex motion having an anticlockwise rotation. For $x/D = 1$ and 2, the secondary motion is illustrated in figure 10 by plots of the velocity vectors in these cross-sectional planes. The vectors at $x/D = 1$ show clearly the upward and outward deflection of the crossflow by the bent-over jet and the formation of a vortex with anticlockwise rotation. At $x/D = 2$, the superposition of the downward motion on this vortex is evident.

For $R = 1$ the V-velocity over the exit assumes of course rather large values, as can be seen from figure 11. Also, in this case more fluid leaves the pipe near the downstream part of the exit, but the V-distribution over the exit is now more uniform than in the case of $R = 0.5$. At $x/D = 2$, the bending over of the jet is almost complete so that there is only a small normal velocity at that station. Further downstream, the downwash effect caused by the wake region sets in so that, on average, a negative V-component has been measured. Superimposed is the bound vortex motion, which is directed away from the wall, but it appears that the downwash effect is stronger.

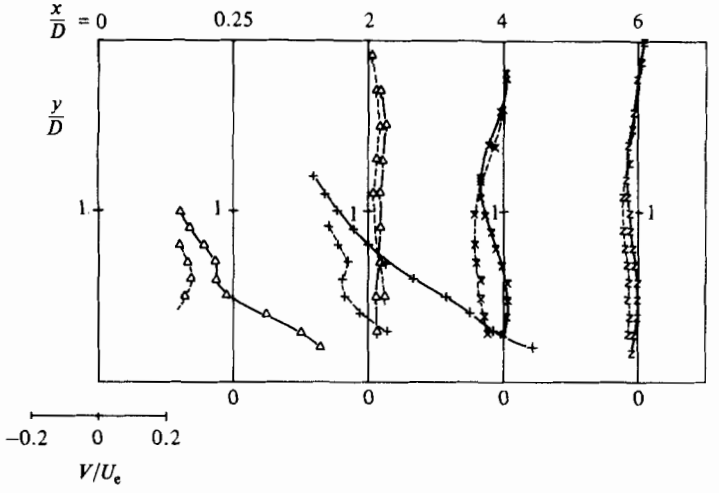

FIGURE 11. Mean V-velocity profiles for $R = 1$ at $z/D = 0$ and $z/D = -0.5$; symbols as in figures 5 and 8.

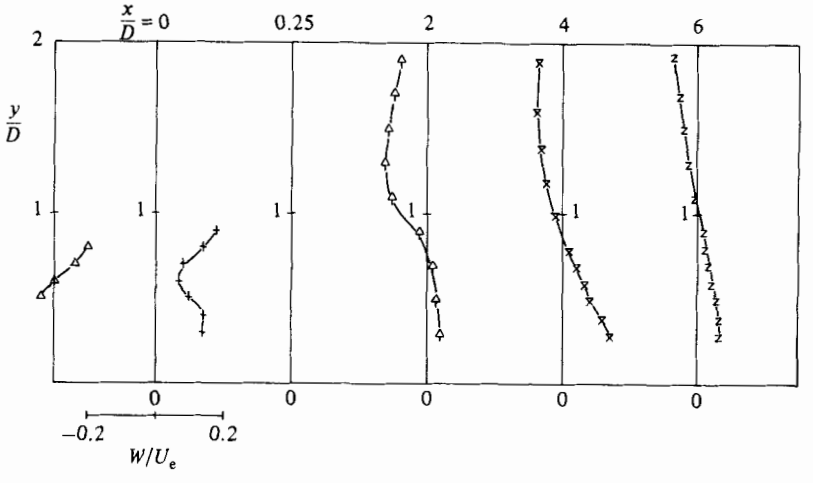

FIGURE 12. Mean W-velocity profiles for $R = 1$ at $z/D = -0.5$; symbols as in figure 5.

The W-velocity profiles in figure 12 show again rather large negative values in the exit region which are due to the deflection of the crossflow round the jet.

The maximum of the outward motion is now further away from the wall because the jet penetrates further into the crossflow than in the case of $R = 0.5$. Downstream of the exit, an inflow develops near the wall, and an outflow exists further away, being consistent with the bound-vortex motion. The development of this motion can be seen clearly in the vector plots of figure 13. The vortex persists further downstream than in the case of $R = 0.5$, and is certainly still present at the last measurement station ($x/D = 6$).

In the case of the velocity ratio $R = 2$, measurements were carried out only downstream of the exit. The V-profiles shown in figure 14 and the vector plots of figure 16 below indicate a rather complex secondary-flow behaviour. At $x/D = 4$, the jet is still not completely bent over, as can also be seen from the U-profile of figure 7.

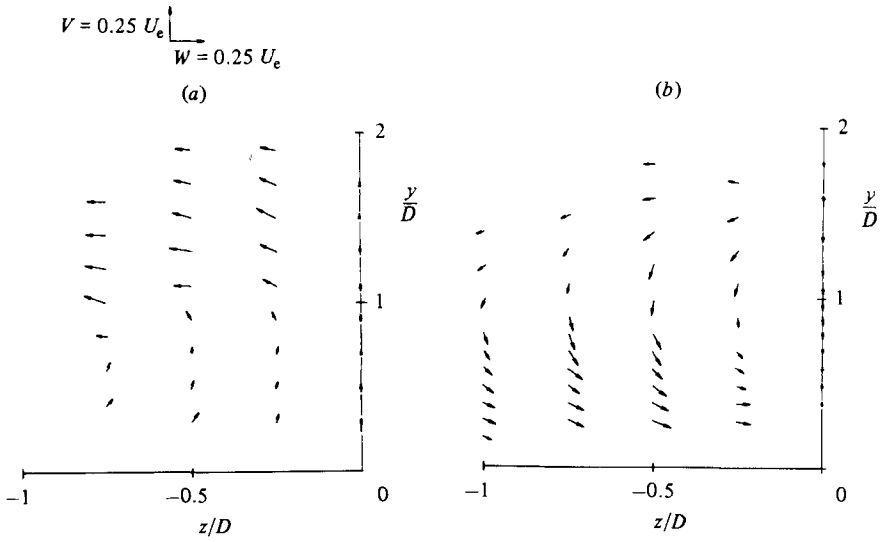

FIGURE 13. Secondary-motion velocity vectors for $R = 1$, at planes (*a*) $x/D = 2$, (*b*) $x/D = 4$.

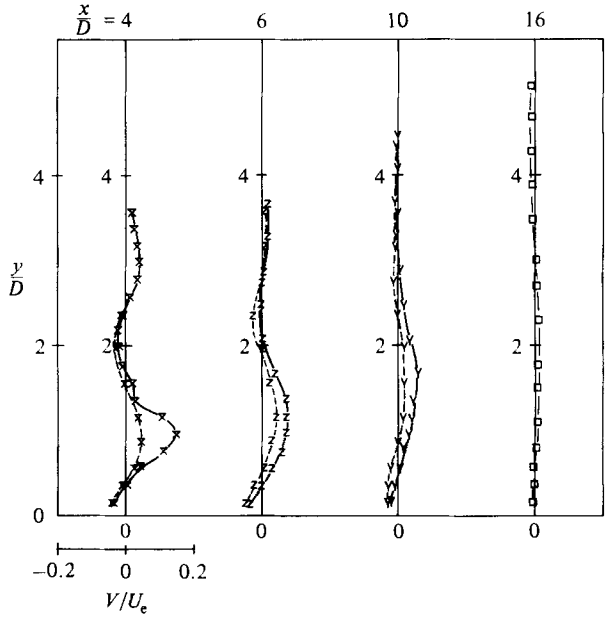

FIGURE 14. Mean V-velocity profiles for $R = 2$ at $z/D = 0$ and $z/D = -0.5$; symbols as in figures 5 and 8.

As a consequence, a positive V-velocity is present at around $y/D = 3$. Also, in this case the wake region is not near the wall, as the near-wall region is occupied by a wall-jet flow. At $x/D = 4$, the wake region is at around $y/D = 1.7$ and moves further away from the wall as one goes in the downstream direction. The wake-region core induces downward motion of the fluid above it and upward motion of the fluid beneath it, which explains the negative V-velocities around $y/D = 2$ and the positive V-velocities at $y/D \approx 1$. The upward motion can also be associated with the bound vortex, whose strength increases with the velocity ratio. This upward velocity carries

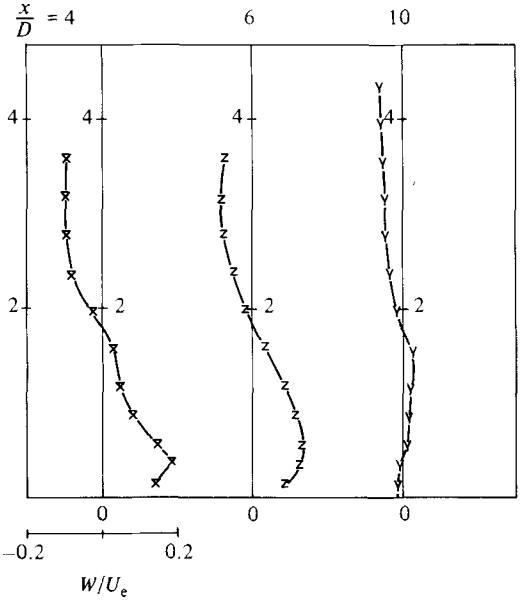

FIGURE 15. Mean W-velocity profiles for $R = 2$ at $z/D = -0.5$; symbols as in figure 5.

higher-momentum fluid from the wall-jet flow upwards to remove the velocity deficit in the wake. Very near the wall, the V-velocity goes negative, which indicates the existence of a vortex counterrotating to the bound vortex. However, there were not sufficient measurement points to resolve the second vortex in the vector plots. The W-profiles in figure 15 show clearly the bound-vortex motion. It is also interesting to see that W decreases near the wall, and even goes negative at $x/D = 10$. This supports the notion that there is a counterrotating vortex near the wall; perhaps W goes negative very near the wall also at $x/D = 4$ and 6, but the first measurement point was simply too far away from the wall to detect this. Both the V- and the W-velocity profiles indicate that the secondary motion is already quite weak at $x/D = 10$, indicating that the bound vortex decays fairly fast. The presence and decay of this vortex can also be seen clearly from the vector plots of figure 16.

From the U- and V-component measurements, the streamline picture at the symmetry plane ($z = 0$) was constructed for the case of $R = 0.5$ and is shown in figure 17. This figure illustrates convincingly the strong interaction of jet and crossflow in the exit region which can be considered as equivalent to placing a partial cover over the jet exit. The jet bending can be seen to start already inside the pipe and is virtually completed at the downstream end of the exit ($x/D = 0.5$). Also illustrated in the figure is the lifting of the cross-stream over the bent-over jet. The separation of the oncoming boundary layer is also shown by way of the vortex just upstream of the exit, which forms the origin of the horseshoe vortex. Some pipe fluid was observed to be entrained into this vortex as indicated in the figure. Also indicated in the figure is the effect of streamline curvature on the turbulence. A minus is attached to the streamlines when curvature is stabilizing, that is when the velocity increases in the positive direction of the radius of curvature, and a plus sign is attached to those parts of the streamline where the velocity decreases in the direction of the radius of curvature so that the effect is destabilizing.

A more quantitative picture of the streamline curvature is presented in figure 18,

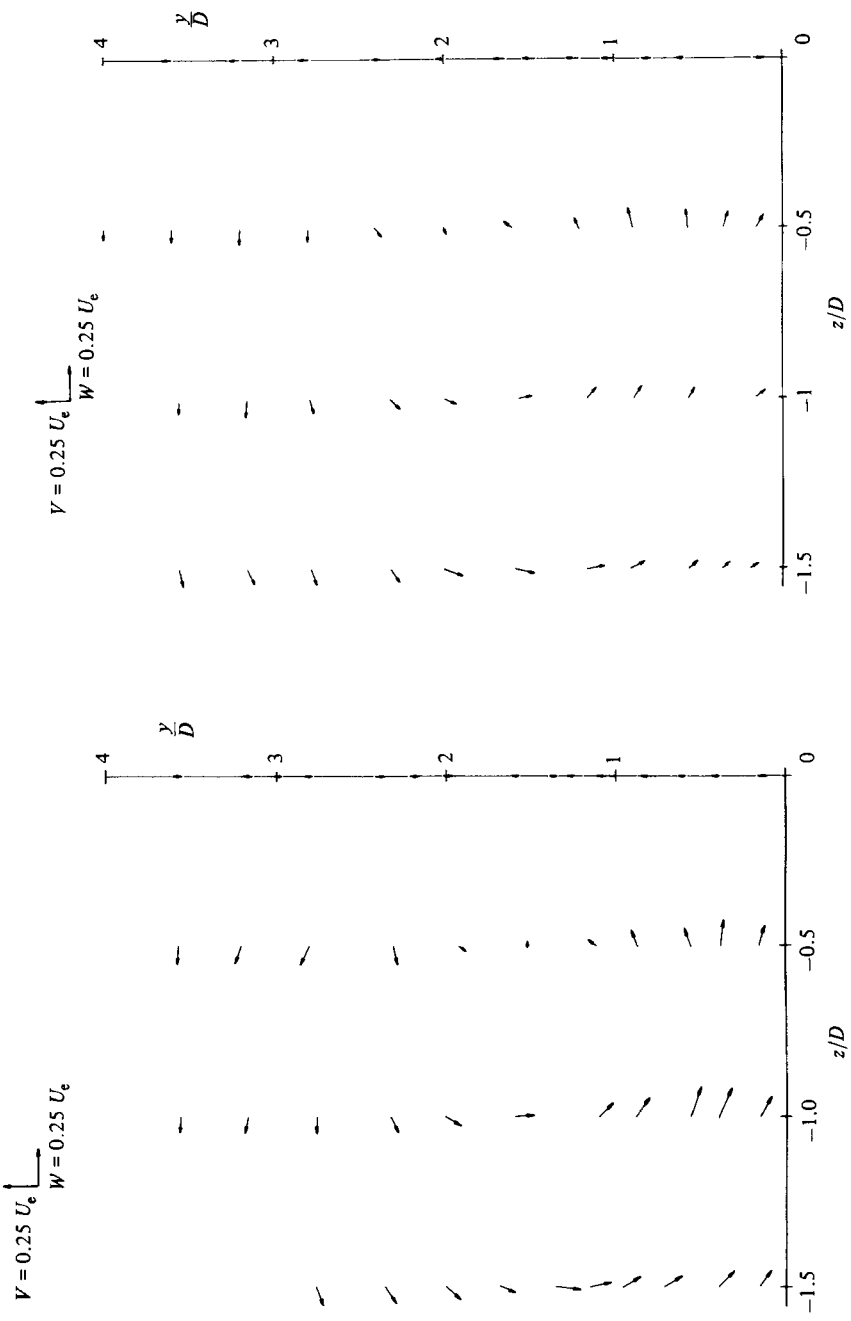

FIGURE 16. Secondary-motion velocity vectors for $R = 2$ at planes (*a*) $x/D = 4$, (*b*) $x/D = 6$.

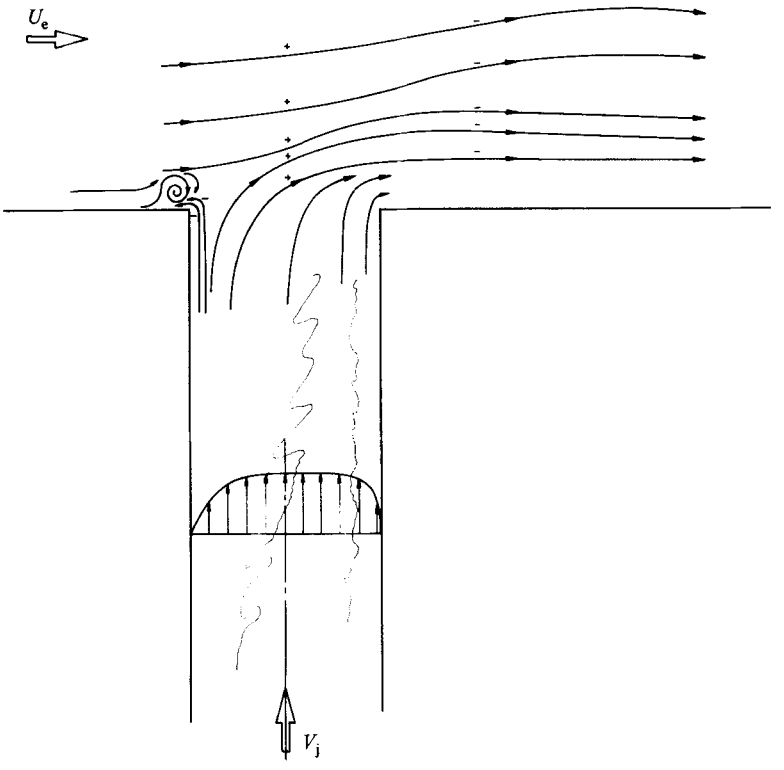

FIGURE 17. Streamline picture for $R = 0.5$ at $z/D = 0$: (+) unstable; (−) stable curvature.

where the profiles of the radius of curvature are given for the situation considered in figure 17 for several downstream stations. For the two stations $x/D = 0$ and 1, the stability parameter

$$S = \frac{\partial V/\partial x}{\partial U/\partial y},$$

introduced by Bradshaw (1973) is also given. The curvature $1/r$, where r is the radius of curvature, was determined from the change of the velocity angle α in the streamwise direction s with the aid of the following equation:

$$\frac{1}{r} = \frac{\mathrm{d}\alpha}{\mathrm{d}s} = \frac{\partial\alpha}{\partial x}\frac{\partial x}{\partial s} + \frac{\partial\alpha}{\partial y}\frac{\partial y}{\partial s}.$$

The gradients of the angle α with respect to x and y and also the gradients $\partial x/\partial s$ and $\partial y/\partial s$ can be determined without difficulty from the available U- and V-velocity measurements. The curvature is positive when the streamlines bend upwards and negative when they bend downwards. Figure 18 shows fairly high negative values of curvature as the jet bends around and positive values in the initial region of the lifting of the crossflow over the jet. At $x/D = 1$, the curvature is already much smaller, and at $x/D = 2$ it has almost disappeared. The stability parameter S behaves as has already been indicated in figure 17. The bending over of the jet is associated mainly with a destabilising effect so that turbulence tends to be increased. Downstream of the exit, at $x/D = 1$, the curvature then acts to stabilize and hence to damp turbulence.

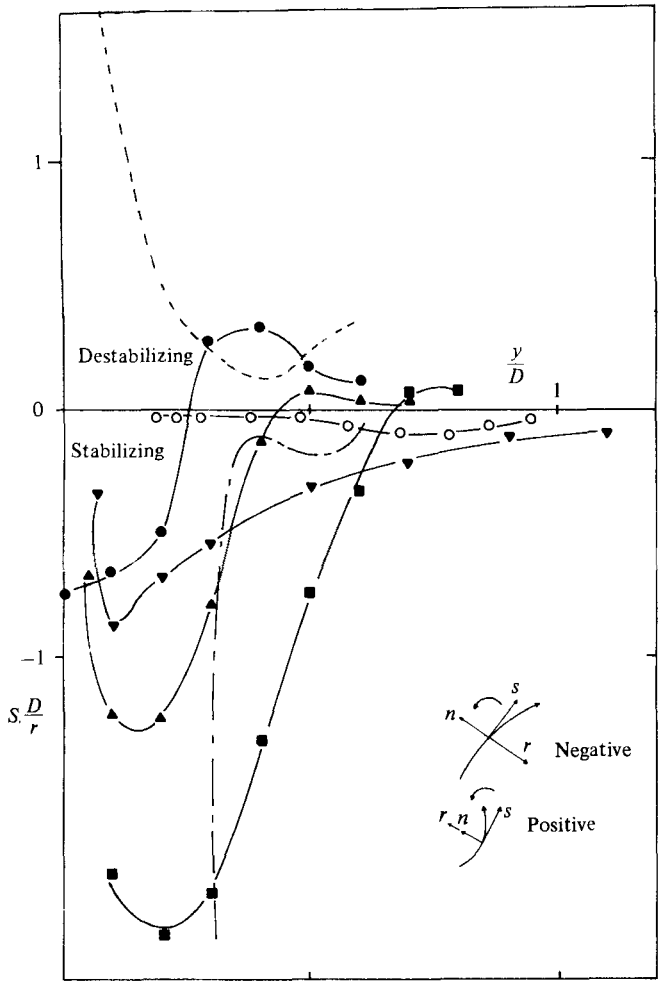

FIGURE 18. Mean streamline curvature plots at $z/D = 0$ for $R = 0.5$ and at: ●, $x/D = 0$; ▲, 0.25; ■, 0.5; ▼, 1.0; ○, 2.0. ------, stability parameter $S = (\partial V/\partial x)/(\partial U/\partial y)$ at $x/D = 0$; ———, S at $x/D = 1$.

4.2. *Turbulent kinetic energy*

Figures 19, 20 and 21 show the profiles of the turbulent kinetic energy $\frac{1}{2}\overline{q^2} = \frac{1}{2}(\overline{u^2}+\overline{v^2}+\overline{w^2})$ for the three velocity ratios $R = 0.5$, 1 and 2 respectively. Again, the most detailed measurements in the exit region were taken for the lowest velocity ratio $R = 0.5$, and these results, plotted in figure 19, are discussed first. The development of $\overline{q^2}$ can be separated into three regions, the first one being over the exit with various velocity gradients and high curvature being present, the next one being immediately downstream with high production due to the velocity gradient $\partial U/\partial y$, and in the last region q^2 starts to decay as the mean-velocity gradients become smaller.

In the first region over the exit, the $\overline{q^2}$ distribution is governed by an interaction of different mechanisms: $\overline{q^2}$ is transported into this region from the upstream boundary layer and pipe flows, $\overline{q^2}$ is produced and perhaps locally also destroyed by various mean-velocity gradients, notably $\partial U/\partial y, \partial V/\partial x, \partial W/\partial z$, and the turbulence is subjected to strong streamline curvature. It appears, however, that the production

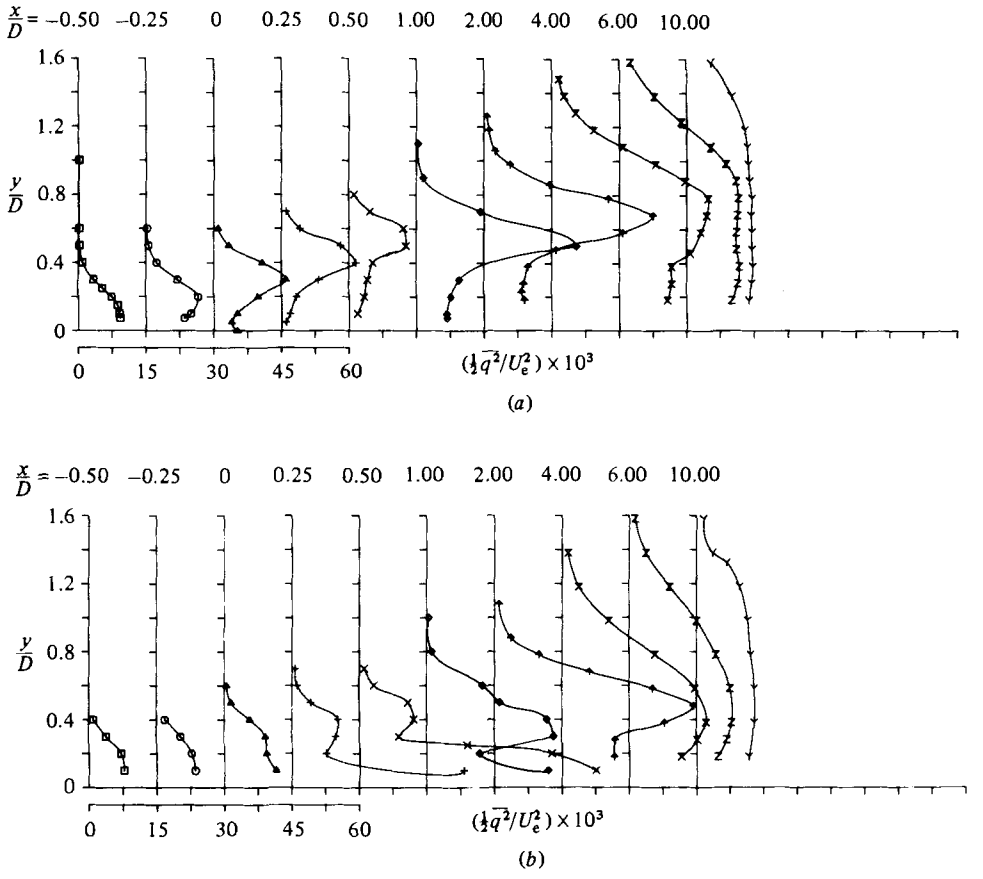

FIGURE 19. Turbulent-kinetic-energy profiles for $R = 0.5$ at (*a*) $z/D = 0$, (*b*) $z/D = -0.5$; symbols as in figure 5.

due to the mean-velocity gradient $\partial U/\partial y$ is the dominant process, because a close correlation can be observed between $\overline{q^2}$ and $\partial U/\partial y$. As the maximum of the velocity gradient moves in the positive y-direction, so does the maximum of the $\overline{q^2}$ profile. Downstream of the exit, the velocity gradient $\partial U/\partial y$ becomes significantly larger in the shear layer above the wake region (see figure 5*a*), and these gradients generate high values of $\overline{q^2}$ in the shear-layer region. Again, the position of the maximum of $\overline{q^2}$ corresponds roughly to the position of the largest velocity gradient, but the streamline convergence (near the wall) and divergence (away from the wall, see figure 9) has also an influence on the $\overline{q^2}$ production. For example, at $x/D = 1$ the production by $\partial W/\partial z$ is 50% of the production by $\partial U/\partial y$. Further downstream, the wake behaviour disappears and so do the strong $\overline{q^2}$ gradients; as a result, less kinetic energy is produced and that having been produced further upstream is convected downstream and diffused by the turbulent motion towards the wall. At $x/D = 10$, the $\overline{q^2}$ level is already much lower.

Figure 19(*b*) shows the development of the $\overline{q^2}$ profile in the plane $z/D = -0.5$. At the first two x-stations, the profiles correspond to those in boundary layers and seem not to have been influenced by the jet. This influence starts at $x/D = 0$, indicating the development of two peaks in the $\overline{q^2}$ profile. Again, these two peaks correspond closely to the U-profile (see figure 5*b*), which shows two maxima of the

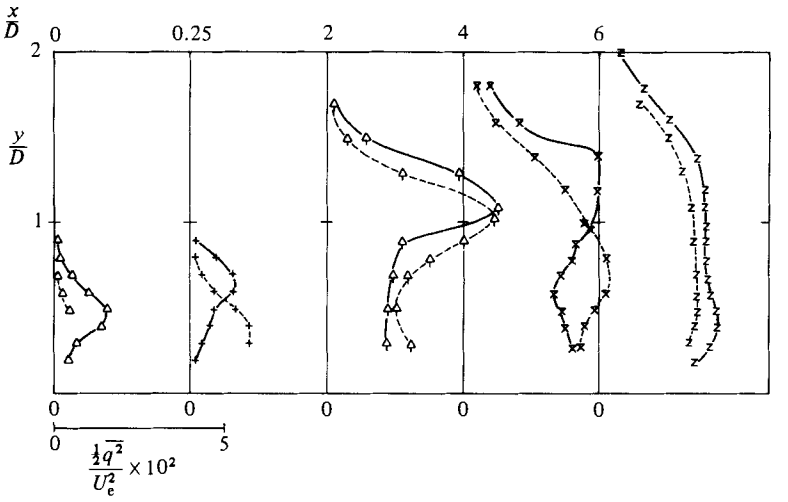

FIGURE 20. Turbulent-kinetic-energy profiles for $R = 1$: solid lines $z/D = 0$, dotted lines $z/D = -0.5$.

velocity gradient in the region $0 \leqslant x/D \leqslant 2$ (a third maximum even closer to the wall is outside the measurement range). The fairly steep increase of the velocity near the wall, which was discussed above, generates fairly large values of $\overline{q^2}$. The second peak is related to the shear layer between jet and freestream which starts to form, for this z-plane, at around $x/D = 0.25$. This behaviour of the second maximum is similar to the one discussed for the centreplane ($z/D = 0$), only that the maxima are located closer to the wall, as are the maxima of the velocity gradient $\partial U/\partial y$. Although $\partial U/\partial y$ is the predominant gradient in producing turbulence, the role of the lateral gradient $\partial W/\partial z$ should not be underestimated in this process, particularly not in the regions immediately downstream of the exit. In the wake-like region where the streamlines converge ($\partial W/\partial z < 0$), turbulence production is reduced. In the shear-layer region, the streamlines diverge considerably and turbulence production is increased.

For the case $R = 1$ shown in figure 20, the initial development of $\overline{q^2}$ over the exit is not much different from the one for $R = 0.5$. The freestream velocities are identical and the velocity gradients also comparable in this region, so that roughly the same level of $\overline{q^2}$ is established, the maximum being at larger y-positions in the case of the higher velocity ratio because the jet penetrates further and, as a consequence, the velocity maxima are located higher above the exit. Downstream of the exit, at $x/D = 2$, the maximum $\overline{q^2}$ level is higher than that in the case of $R = 0.5$ because the velocity gradient is considerably steeper at that location for $R = 1$. Here a relatively intense shear layer has developed above the wake region. In the latter, the $\overline{q^2}$ level is only about one-third of the peak level, but, when non-dimensionalized with the square of the local velocity, the $\overline{q^2}$ level in the low-velocity wake region is actually significantly higher than in the bordering shear layer. The kinetic energy generated in the shear layer diffuses towards the wall and 'fills' the wake region; at $x/D = 4$ there is even a tendency for $\overline{q^2}$ to rise towards the wall, and this is associated with the increase of U as the wall is approached. This phenomenon is more pronounced at the higher velocity ratio $R = 2$ and will be discussed below. In general, the gradients at $x/D = 4$ are already smaller than further upstream, so that $\overline{q^2}$ starts to decay, a process which can be seen to continue at $x/D = 6$, where diffusion has evened out the $\overline{q^2}$ profile over most of the region between the wall and the edge of the bent-over jet.

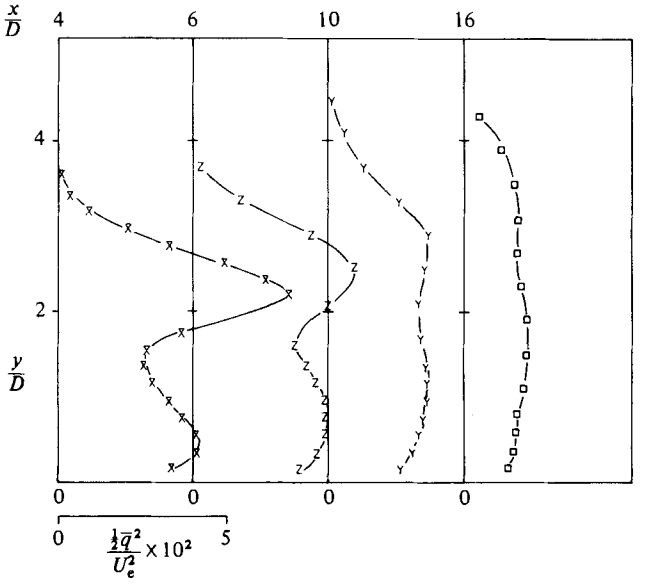

FIGURE 21. Turbulent-kinetic-energy profiles for $R = 2$ at $z/D = 0$.

The $\overline{q^2}$ profiles at $z/D = -0.5$ also included in figure 20 show a maximum near the wall in the exit region which is associated with the oncoming boundary layer swept around the jet and the fairly strong W-gradients resulting from this. Further downstream, the shear layer has spread to this z-plane and here the development is rather close to that at the symmetry plane.

For the largest velocity ratio, $R = 2$, the kinetic-energy profiles are shown in figure 21. The double peak behaviour is here more pronounced than in the case of $R = 1$, because the velocity profile (see figure 7) also shows a much stronger increase in velocity near the wall which causes the flow to assume wall-jet character in this region. The gradients $\partial W/\partial z$ also contribute to the generation of $\overline{q^2}$, and there appears to be also transport of $\overline{q^2}$ from outer regions by the inward W and in addition diffusion, so that the location of the $\overline{q^2}$ peak near the wall is rather at the location of the velocity maximum than of the maximum of the velocity gradient. As the double-peak nature of the velocity profile disappears further downstream, so does that of $\overline{q^2}$. At $x/D = 16$ the velocity gradients are quite low, and $\overline{q^2}$ has decayed already considerably, being again fairly uniformly distributed over the region in which the velocity deviates from the freestream velocity.

4.3. *Turbulent shear stresses*

Profiles of the turbulent shear stress $\overline{uv}$ are presented in figures 22–24 for the same downstream and spanwise locations and velocity ratios for which the turbulent-kinetic-energy profiles were presented. As in the case of $\overline{q^2}$ profiles, the maxima of the uv-profiles correspond closely to the positions of the maxima of the velocity gradient $\partial U/\partial y$. The reason for this is that the correlation $\overline{uv}$ is mainly produced by the product $\overline{v^2}\,\partial U/\partial y$, as can be seen from the balance equation governing $\overline{uv}$. Figure 22(*a*) shows the development of the $\overline{uv}$-profiles for $R = 0.5$ at the centreplane. This development is in fact very similar to that of the turbulent kinetic energy (figure 19*a*). The maximum shear-stress value increases as the shear layer over the wake region develops and the velocity gradients are built up, and the maximum of $\overline{uv}$ decreases

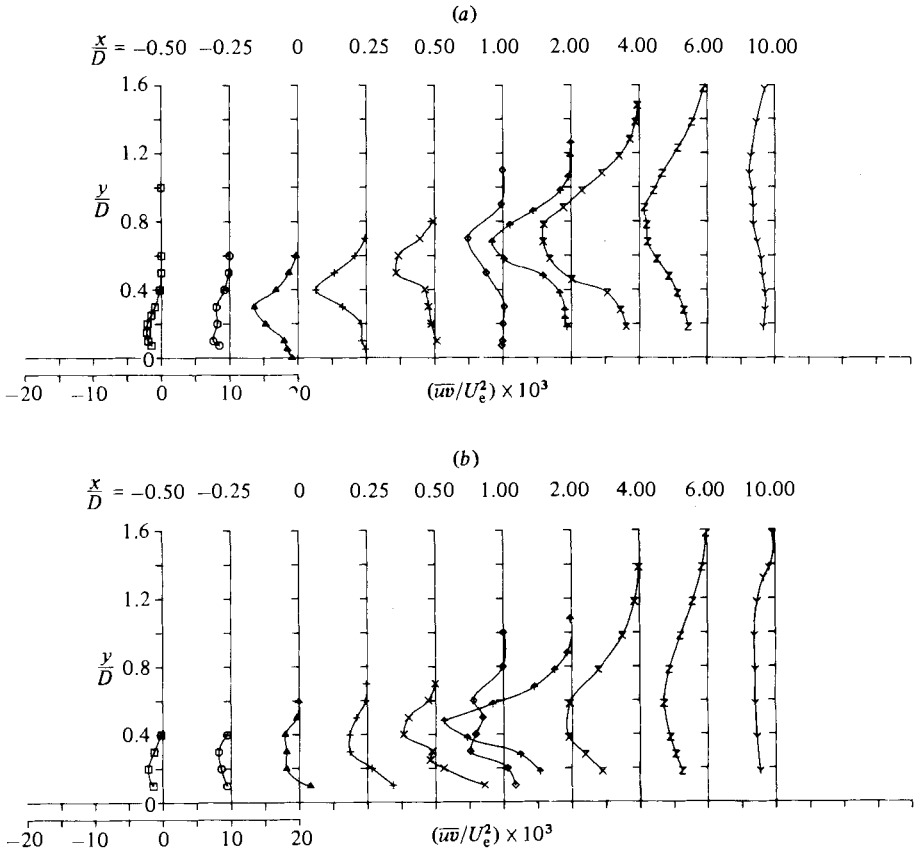

FIGURE 22. $\overline{uv}$-shear-stress profiles for $R = 0.5$ at (*a*) $z/D = 0$, (*b*) $z/D = -0.5$; symbols as in figure 5.

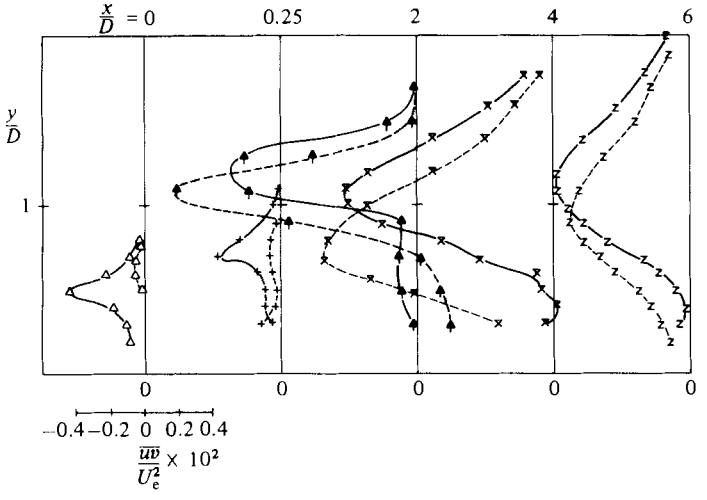

FIGURE 23. $\overline{uv}$-shear-stress profiles for $R = 1$: solid line $z/D = 0$, dotted line $z/D = -0.5$.

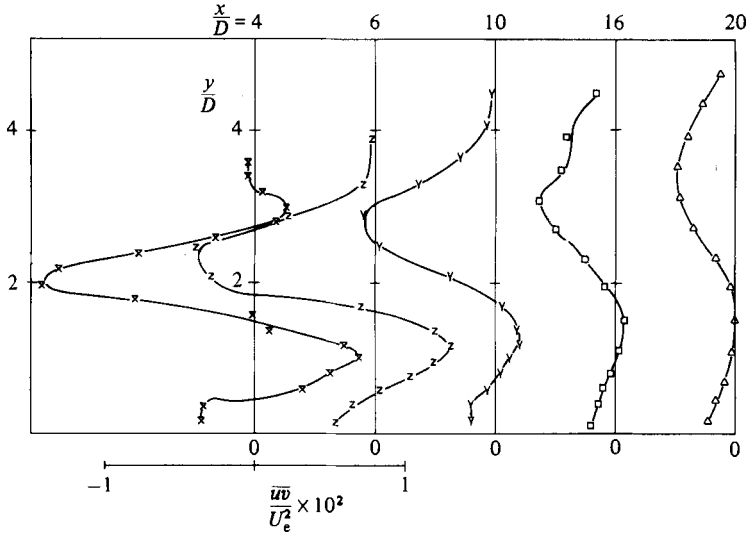

FIGURE 24. $\overline{uv}$-shear-stress profiles for $R = 2$ at $z/D = 0$.

again as the velocity gradients become smaller further downstream. However, the largest value of $\overline{uv}$ cannot be found at $x/D = 2$, where the largest velocity gradient was observed, but at the next downstream station $x/D = 4$. The further increase in shear stress from $x/D = 2$ to $x/D = 4$ is due to the interaction in the production process between velocity gradient and the normal fluctuations v which are still being built up, and also due to the convection of the correlation $\overline{uv}$ produced further upstream. In the wake region the shear stress $\overline{uv}$ is quite small, also relative to the turbulent kinetic energy $\overline{q^2}$. This is further made evident in figure 25, which shows the ratio of $\overline{uv}$ to $\overline{q^2}$, sometimes referred to as structure parameter. The wake region with its fairly uniform velocity does not have typical shear-layer character, which explains why the shear stress is relatively small. Further, the flow in this region was subjected to strongly stabilizing curvature as it left the pipe at the rear part (see figure 17). It is well known that the curvature reduces the shear stress more than the turbulent kinetic energy, and the strong curvature may have wiped out the shear stress altogether. On the other hand, in the forward part of the exit hole the curvature is destabilizing, and this offers an explanation for the fairly high value of $2\overline{uv}/\overline{q^2}$ at $x/D = 0$, particularly at relatively small y-values, where the destabilizing effect is strongest. In the outward shear-layer region, the value of the structure parameter can be seen to be close to 0.3, that is the value found usually in undisturbed shear layers. Further downstream, there is a tendency for the parameter to adopt this value over a large range in the y-direction, developing towards the situation found in a boundary layer. It may also be observed from figure 25 that $\overline{uv}$ builds up more slowly than $\overline{q^2}$ in the past-wake region near the wall. It seems that $\overline{uv}$ diffuses less rapidly from the shear-layer region towards the wall than does $\overline{q^2}$, and also there is less convection from upstream because of the very small $\overline{uv}$-values in the initial wake region.

Figure 22 (*b*) shows the corresponding shear-stress profiles at the plane $z/D = -0.5$. At several downstream stations, the shear-stress profiles can be seen to change sign, which is in accordance with the velocity profiles shown in figure 8 (*b*), where the

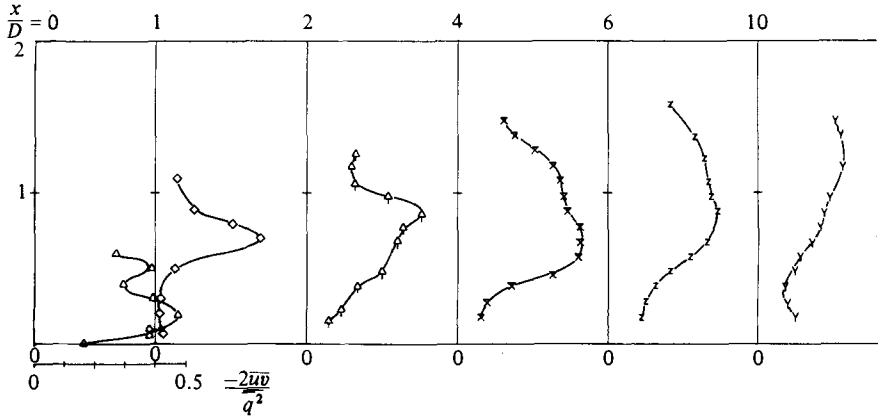

FIGURE 25. Structural parameter $-2\overline{uv}/\overline{q^2}$ for $R = 0.5$ at $z/D = 0$.

velocity gradient also changes sign near the wall. In the outer shear-layer region, the development of $\overline{uv}$ is similar to that at the centreplane.

For the case of $R = 1$ (figure 23) the initial build-up of the shear stress is somewhat slower than in the case of $R = 0.5$ because the initial velocity gradients are smaller. Downstream of the exit, however, the development of $\overline{uv}$ is fairly fast because $\partial U/\partial y$ becomes large quite quickly. As the velocity profile with a change of sign in $\partial U/\partial y$ develops at $x/D = 2$ and further downstream, $\overline{uv}$ also tends to change sign, but does not do so at all locations at which $\partial U/\partial y$ changes sign (e.g. at $x/D = 6$). There are therefore regions where shear stress and velocity gradient have opposite sign so that a negative eddy viscosity results; these regions cannot be simulated realistically by an eddy-viscosity model.

The shear-stress profile for the case $R = 2$ shown in figure 24 can be seen to change sign several times. At $x/D = 4$, the streamwise velocity exceeds the freestream velocity near the outer edge, and the velocity profile has three extremes; the shear-stress profile therefore changes sign three times, roughly at their location. Further downstream, the velocity is always smaller than the freestream velocity, so that one maximum in the U-profile has disappeared and $\overline{uv}$ changes sign only twice. The shear-stress values are largest in the outer shear-layer region, but they are also fairly significant in the wall-jet-like region. When this and the wake region start to disappear further downstream, the shear-stress profile stops changing sign and develops towards a profile typical for boundary-layer flow.

In general, the shear stress $-\rho\overline{uv}$ and the velocity gradient $\partial U/\partial y$ have the same sign, so that the eddy viscosity $\nu_t = -\overline{uv}/(\partial U/\partial y)$ is positive in most flow regions for all velocity ratios R, and eddy-viscosity models should in principle be capable of simulating the shear-stress distribution (for the example of $R = 0.5$ see figure 26). However, the eddy-viscosity variation itself is rather complex in these flows so that no simple eddy-viscosity model can be expected to work well.

Correlations of velocity fluctuations containing an odd power of the lateral velocity w are zero at the plane of symmetry ($z/D = 0$), and hence the measured shear stresses $\overline{uw}$ and $\overline{vw}$ should be zero at that plane. Typically, the measured values of $\overline{uw}$ and $\overline{vw}$ at $z/D = 0$ were 5 to 10 times less than the measurements at $z/D = -0.5$, which creates further confidence in the accuracy of the triple-wire measurements. In contrast, the only existing detailed turbulence measurements, namely those of Crabb *et al.* (1981) failed to meet the symmetry conditions mentioned above. At $x/D = 8$,

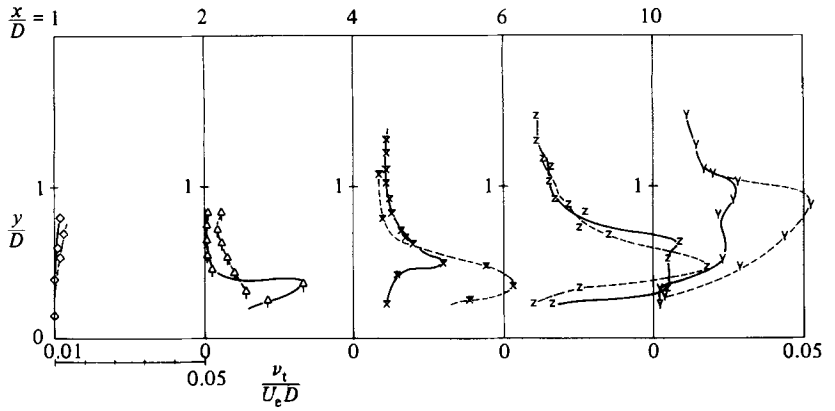

FIGURE 26. Eddy viscosity $\nu_t = -\overline{uv}/(\partial U/\partial y)$ for $R = 0.5$ at $z/D = 0$; symbols as in figure 5.

the $\overline{uw}$-profile of Crabb *et al.* shows a maximum at $z/D = 0$ (see their figure 7*a*), which casts some doubt on the accuracy of their turbulence measurements. It should further be mentioned that these authors did not measure the shear stress $\overline{vw}$.

The shear stress $\overline{uw}$ represents the lateral turbulent mixing and governs the lateral spreading of the bent-over jet. The production terms in the transport equation for this stress read

$$P_{\overline{uw}} = -\overline{u^2}\frac{\partial W}{\partial x} - \overline{uv}\frac{\partial W}{\partial y} - \overline{uw}\frac{\partial W}{\partial z} - \overline{uw}\frac{\partial U}{\partial x} - \overline{vw}\frac{\partial U}{\partial y} - \overline{w^2}\frac{\partial U}{\partial z}. \tag{2}$$

Among the U-gradient terms, the one with $\partial U/\partial z$ is the dominant one. For all velocity ratios, this gradient is negative (for $z < 0$), so that this gradient produces a positive contribution towards $\overline{uw}$ according to (2). This equation shows that gradients of the component W in all three directions also contribute to the production of $\overline{uw}$. Among these, the production due to $\partial W/\partial y$ appears to be the most important one because $\partial W/\partial y$ is by far the largest gradient, particularly near the wall.

Figure 27(*a*) shows the measured $\overline{uw}$-profiles at $z/D = -0.5$ for $R = 0.5$. At the initial stations ($x/D \leqslant 0$) the level of $\overline{uw}$ is relatively small because the relevant gradients of U and W are small in this region. Starting at $x/D = 0$, a profile develops with positive $\overline{uw}$-values near the wall and near the outer edge and with negative values in between. The positive values are associated mainly with the production due to the velocity gradient $\partial U/\partial z$ as discussed above. Superimposed is the contribution of the production term $-\overline{uv}\,\partial W/\partial y$. As $\overline{uv}$ is predominantly negative (see figure 22*b*), and $\partial W/\partial y$ is negative in the inner region and positive in the outer region down to $x/D = 2$, this production makes a positive contribution in the outer region and a negative one in the inner region, except very near the wall where the shear stress $\overline{uv}$ is positive. The negative production of $\overline{uw}$ is particularly strong at $x/D = 0.5$ (see the strong gradient in figure 9), which explains the large negative $\overline{uw}$-value at that station. Further downstream, the W-gradients become small so that they do not influence significantly the production of $\overline{uw}$, and the gradient $\partial U/\partial z$ is clearly the dominant one, causing $\overline{uw}$ to be positive everywhere in the negative z-domain.

The $\overline{uw}$-profiles for the case with $R = 1$ shown in figure 27(*b*) show a similar behaviour. $\overline{uw}$ is again predominantly positive owing to the generation by $\partial U/\partial z$, and the gradient $\partial W/\partial y$ causes $\overline{uw}$ to be negative in some regions, which in this case are further away from the wall than for $R = 0.5$ since the location of the maximum

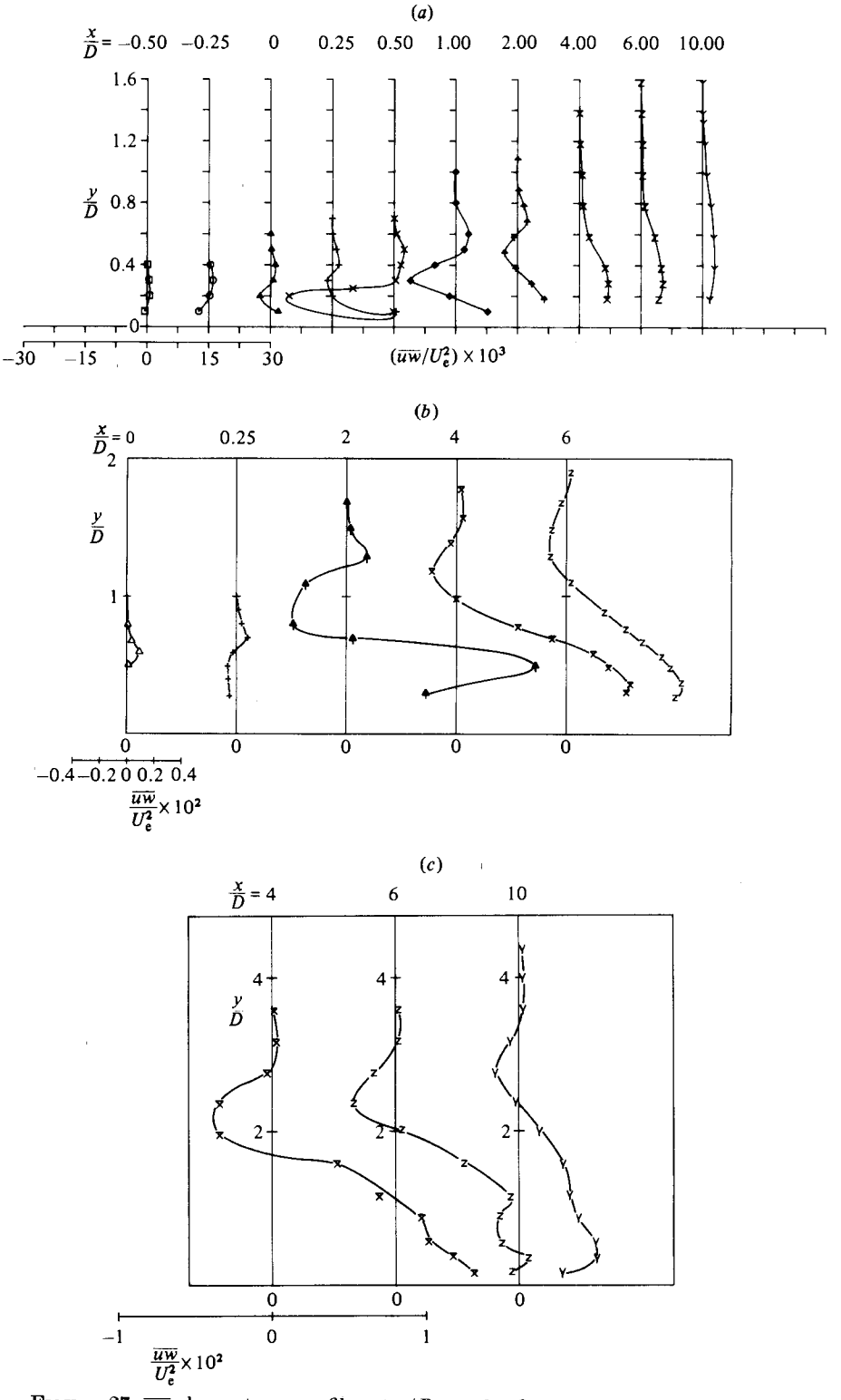

FIGURE 27. $\overline{uw}$-shear-stress profiles at $z/D = -0.5$ for (*a*) $R = 0.5$, (*b*) 1, (*c*) 2; symbols as in figure 5.

negative $\partial W/\partial y$ is also further away. The secondary motion persists longer in this case so that negative $\overline{uw}$-values are still present at $x/D = 6$. Further downstream, however, $\overline{uw}$ will again be entirely positive. The $\overline{uw}$-development for $R = 2$ shown in figure 27 (*c*) is very similar. Here $\partial W/\partial y$ is negative in most regions, so that this gradient makes a negative contribution to $\overline{uw}$ where $\overline{uv}$ is negative and *vice versa*. Indeed, the negative values of $\overline{uw}$ can be seen to occur roughly where $\overline{uv}$ (figure 24) is negative. The situation very near the wall, where $\overline{uv}$ is negative and $\partial W/\partial y$ is positive is not very clear, but it can be seen from (2) that other gradients also have an influence.

The eddy-viscosity relation for the shear stress $\overline{uw}$ reads

$$\overline{uw} = -\nu_t\left(\frac{\partial U}{\partial z}+\frac{\partial W}{\partial x}\right).$$

The experiments indicate that everywhere the gradient $\partial W/\partial x$ is considerably smaller than the gradient $\partial U/\partial z$, so that the above eddy-viscosity relation implies that the shear stress $\overline{uw}$ is closely associated with the gradient $\partial U/\partial z$. The discussion above has shown, however, that this is not the case in certain flow regions in which a negative eddy viscosity would result from the above relation. Simple eddy-viscosity models would therefore not lead to realistic simulation of such regions, and a model is necessary that accounts for the production of $\overline{uw}$ due to the gradient $\partial W/\partial y$.

The shear stress $\overline{vw}$ acts to damp the secondary-vortex motion. The motion is similar to that in free-vortex flows like wing-tip vortices of aeroplanes or swirling jets, where, near the centre, the circumferential velocity increases linearly with distance from the centre as in solid-body rotation while further away it increases less and finally decreases as in a potential vortex. Such a motion is clearly evident also for the bound vortex in the jet in a crossflow and can be seen most clearly from the W-profiles shown in figure 15. In vortex flows, it is the gradient $\partial(W/r)/\partial r$ rather than the gradient of the circumferential velocity itself that generates the circumferential shear stress, in this case $\overline{vw}$. When the rotation is anticlockwise as in the present case, and W increases less than linearly from the vortex centre, the above gradient is positive so that it generates a negative $\overline{vw}$. This explains why the measured $\overline{vw}$-values shown in figure 28 are predominantly negative. However, other gradients contribute to the generation of $\overline{vw}$, which complicates the picture, particularly in the initial region of the jet. The production terms in the $\overline{vw}$ transport equation read

$$P_{\overline{vw}} = -\overline{uv}\frac{\partial W}{\partial x}-\overline{v^2}\frac{\partial W}{\partial y}-\overline{vw}\frac{\partial W}{\partial z}-\overline{uw}\frac{\partial V}{\partial x}-\overline{vw}\frac{\partial V}{\partial y}-\overline{w^2}\frac{\partial V}{\partial z}. \tag{3}$$

In the flow region with a clearly developed vortex flow it is the combination of the terms with the gradients $\partial V/\partial z$ and $\partial W/\partial y$ that generates the shear stress $\overline{vw}$. In a cylindrical coordinate system with the vortex centre as the axis these terms can be combined to yield a term with the above-mentioned gradient of the circumferential velocity. In the initial region, however, the motion in the (y, z)-plane is not of the vortex type; rather it consists predominantly of an outward flow of the free stream around the jet, as can be seen clearly from figure 9. In this region, the gradient $\partial V/\partial z$ is small, and it is mainly the gradient $\partial W/\partial y$ that generates $\overline{vw}$. This gradient is negative in the inner near-wall region and positive in the outer region, and $\overline{vw}$ attains values of the opposite sign in these regions, as can be seen from figure 28 (*a*). Further downstream, at $x/D = 2$, a vortex behaviour develops and $\overline{vw}$ takes on predominantly negative values. The establishment of negative shear stress $\overline{vw}$ can be seen best from

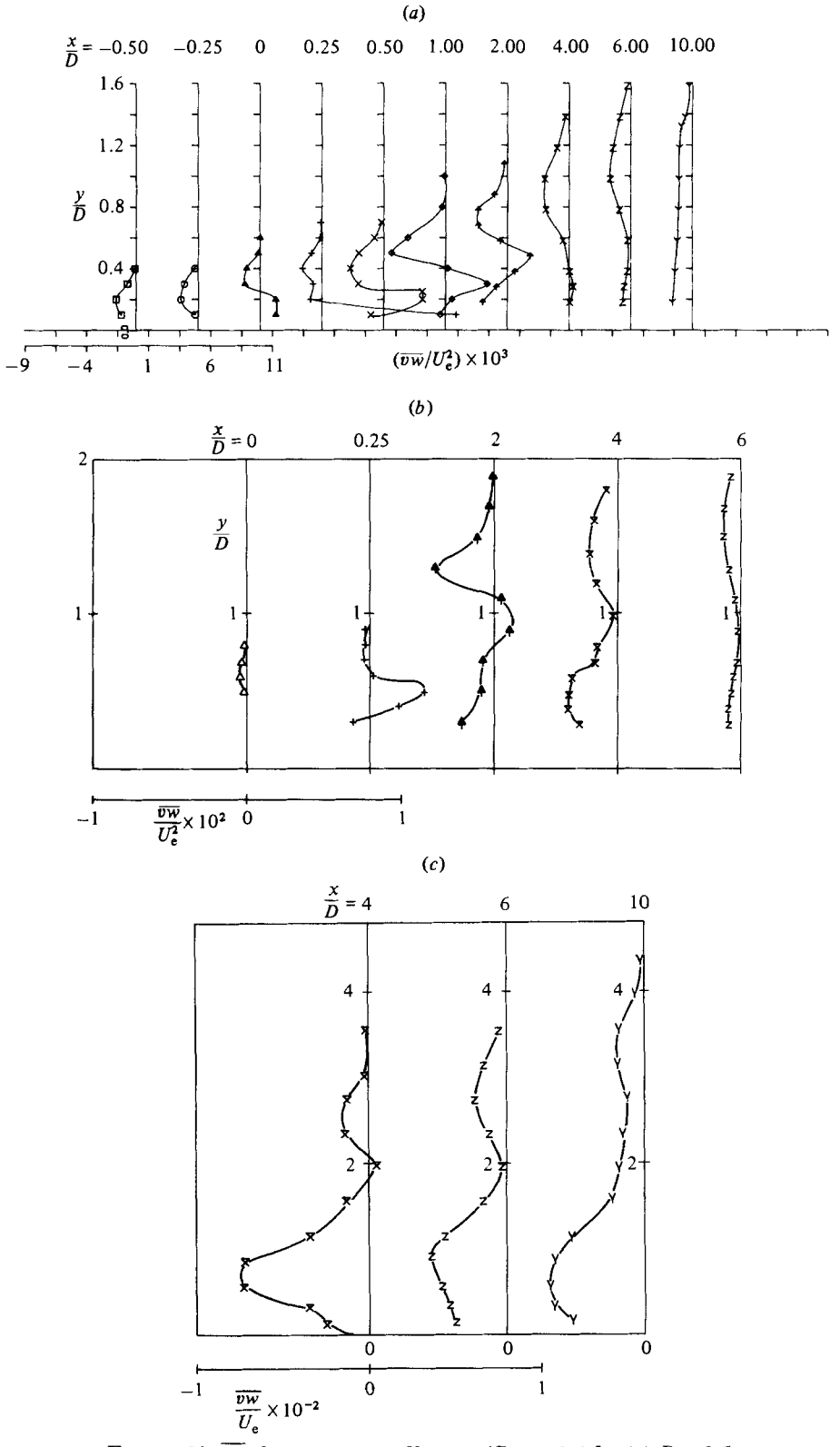

FIGURE 28. $\overline{vw}$-shear-stress profiles at $z/D = -0.5$ for (*a*) $R = 0.5$, (*b*) 1, (*c*) 2; symbols as in figure 5.

the profiles for the higher velocity ratios shown in figures 28(*b*, *c*), where mainly downstream stations are considered at which a clear vortex motion exists. The eddy-viscosity relation for the stress $\overline{vw}$ reads

$$\overline{vw} = -\nu_t\left(\frac{\partial V}{\partial z}+\frac{\partial W}{\partial y}\right),$$

and from the above discussion it can be inferred that the eddy viscosity according to this relation is positive in most regions of the flow, so that an eddy-viscosity model might be suitable for simulating the stress $\overline{vw}$.

4.4. *Turbulent-kinetic-energy balances*

At the symmetry plane ($z/D = 0$), the turbulent kinetic energy equation reads

$$\underbrace{U\frac{\partial \frac{1}{2}\overline{q^2}}{\partial x}+V\frac{\partial \frac{1}{2}\overline{q^2}}{\partial y}}_{\text{advection}}+\underbrace{\overline{uv}\left(\frac{\partial U}{\partial y}+\frac{\partial V}{\partial x}\right)}_{\substack{\text{shear-stress}\\ \text{production}}}+\underbrace{(\overline{u^2}-\overline{v^2})\frac{\partial U}{\partial x}+(\overline{w^2}-\overline{v^2})\frac{\partial W}{\partial z}}_{\text{normal-stress production}}$$

$$+\underbrace{\frac{\partial(\frac{1}{2}\overline{q^2u}+\overline{p'u})}{\partial x}+\frac{\partial(\frac{1}{2}\overline{q^2v}+\overline{p'v})}{\partial y}+\frac{\partial(\frac{1}{2}\overline{q^2w}+\overline{p'w})}{\partial z}}_{\text{diffusion}}+\underbrace{\epsilon}_{\text{dissipation}}=0. \quad (4)$$

This equation is exact, as only terms have been omitted that are zero owing to the symmetry condition at $z = 0$ ($\partial U/\partial z$, $\partial V/\partial z$, $\partial\overline{q^2}/\partial z$, $\overline{uw}$ and $\overline{vw}$). In figures 29–31, the individual terms in the above kinetic-energy equation are presented for the symmetry line at the exit plane and along vertical lines at $x/D = 4$ and 6 for the velocity ratio $R = 0.5$. Attempts have been made to determine all the terms from measurements except the correlations between fluctuating pressure and fluctuating velocities appearing in the diffusion term. The triple velocity correlations in the diffusion term were determined by appropriate evaluation of the hot-wire signals from the three-sensor probe. The dissipation rate ϵ was determined at a limited number of points by analyzing the spectra of velocity fluctuation in the local mean-flow direction (v over exit, u further downstream). In the inertial subrange, the one-dimensional spectrum of u or v is $\Phi = a\epsilon^{\frac{2}{3}}K^{-\frac{5}{3}}$, where a is postulated as a universal constant, taken here to be 0.5 as suggested by Townsend (1976) and K is the streamwise wavenumber. The dissipation rate ϵ has also been determined from the difference of the other terms (neglecting the pressure diffusion), and this will be compared with ϵ obtained from the spectra.

Figure 29(*a*) shows the individual production and advection terms along the centreline of the exit of the jet. Owing to the complexity of the flow at the exit (see figure 17) the production terms could be determined only with an accuracy of about 30%. It is surprising to find that the shear-stress production is considerably smaller than the production due to normal stresses, particularly near the upstream edge of the exit. This is because of the fact that both the velocity gradients $\partial U/\partial y$ and $\partial V/\partial x$ are an order of magnitude smaller than $\partial W/\partial z$. Hence the lateral divergence of the flow in the upstream part of the edge of the exit induces considerable production of turbulent energy. It should be mentioned, however, that the measurements shown in figure 29(*a*) do not include the region very close to the downstream edge where

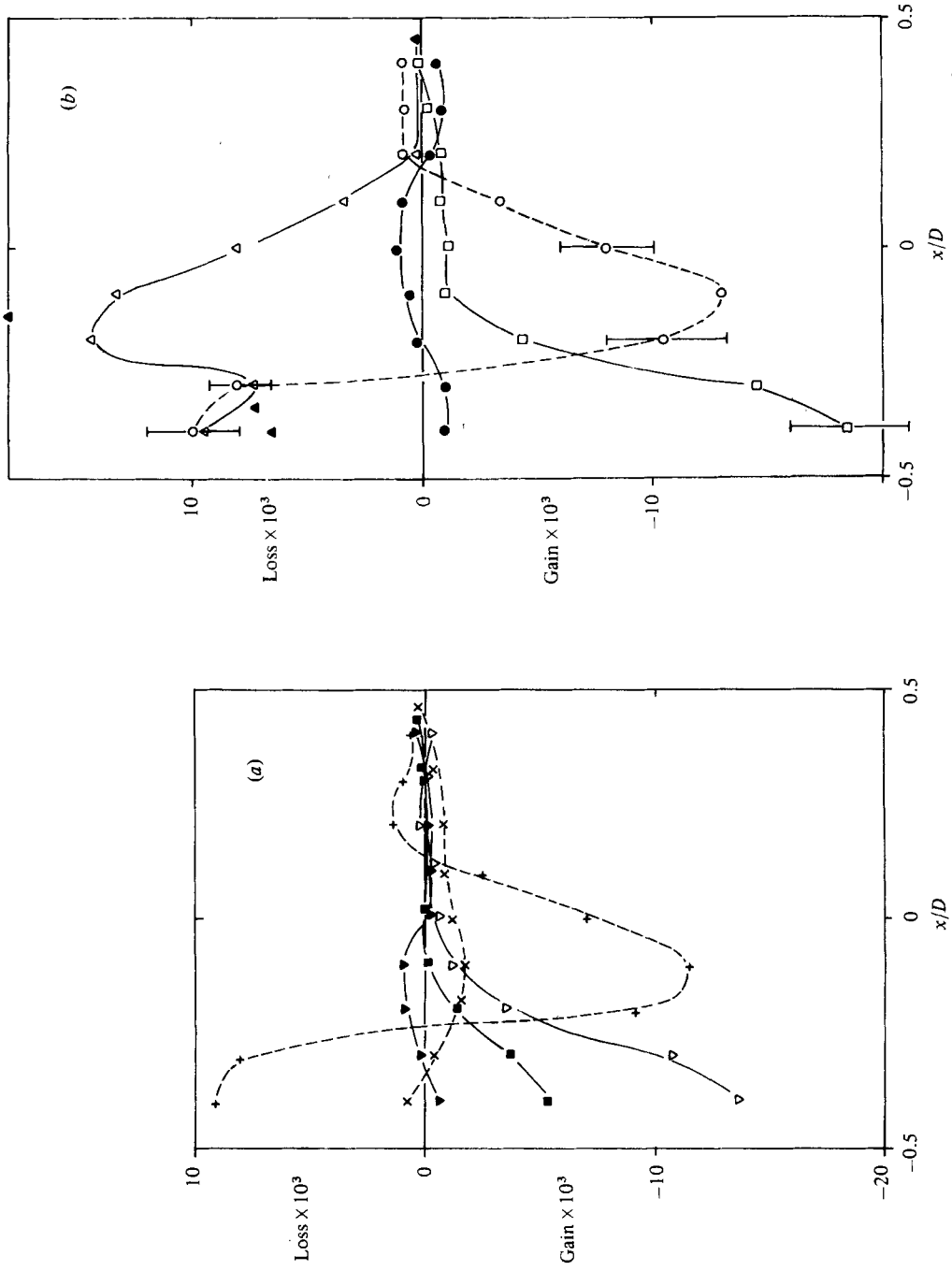

FIGURE 29. (*a*) Turbulent-kinetic-energy production and advection. Subterms at $z/D = 0$ and $y/D = 0$, i.e. over the exit plane, are as follows. Production: ■, $(\overline{u^2} - \overline{v^2})\,\partial U/\partial x$; ▽, $(\overline{u^2} - \overline{v^2})\,\partial W/\partial z$; ▼, $\overline{uv}(\partial U/\partial y + \partial V/\partial x)$. Advection: ×, $U\partial(\frac{1}{2}\overline{q^2})/\partial x$; +, $V\partial(\frac{1}{2}\overline{q^2})/\partial y$. (*b*) Turbulence-kinetic-energy balance at the exit plane: □, production; ○, advection; ●, diffusion; △, dissipation (by difference); ▲, dissipation (measured).

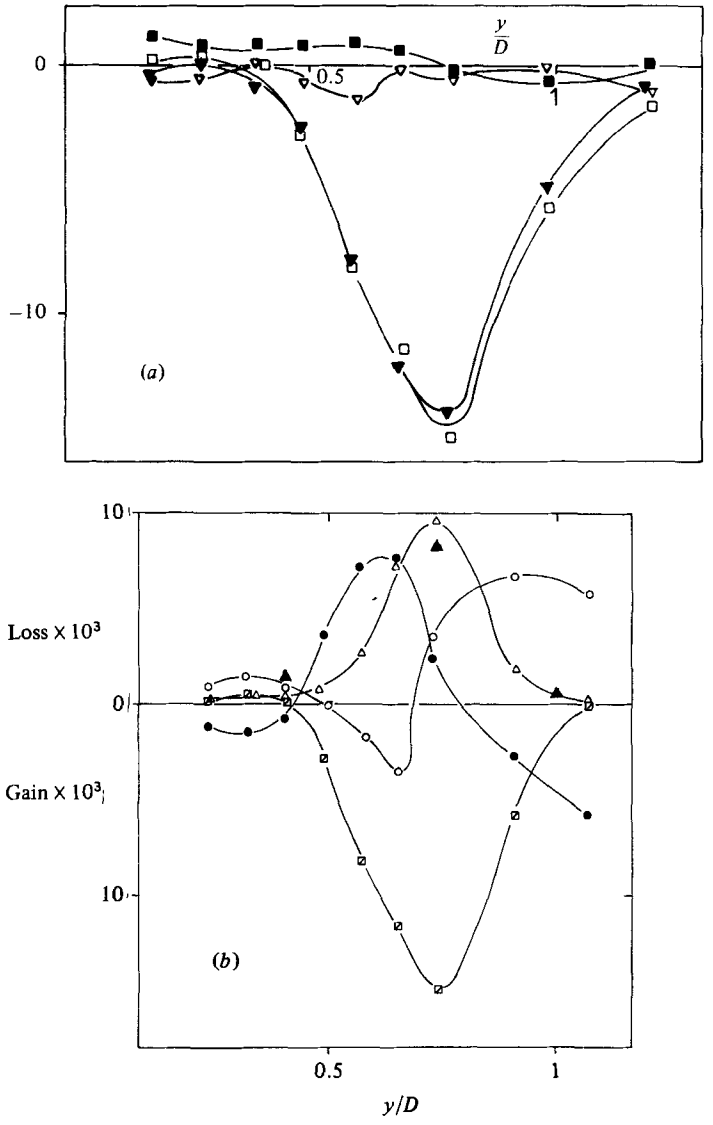

FIGURE 30. (*a*) Production subterms of turbulent kinetic energy for $R = 0.5$ at $z/D = 0$ and $x/D = 4$: □, total production; other symbols as in figure 29(*a*). (*b*) Turbulent-kinetic-energy balance for $R = 0.5$ at $z/D = 0$ and $x/D = 4$; symbols as in figure 29(*a*).

the V-velocity has a very steep negative gradient (the maximum of V is fairly close to the downstream edge), and the shear-stress production is likely to be of significance. Altogether, in the region covered by the measurements there is little production for $x \geqslant 0$. There is even less experimental certainty about the convection terms, particularly the one associated with the vertical velocity and the vertical $\overline{q^2}$ gradient. The latter term could be determined at a few points only, and there is only one point supporting the convection to be negative in the middle region. This negative value follows from the negative $\overline{q^2}$ gradient shown in figure 19 at $x/D = 0$. However, when the rather speculative curve drawn through the convection measurements is used in the kinetic-energy balance to determine the dissipation rate by the difference of the

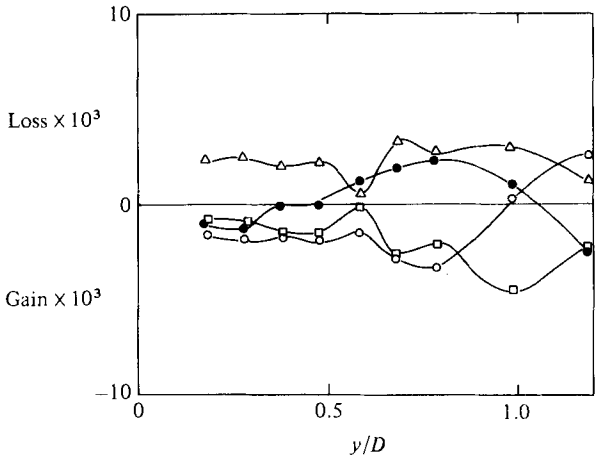

FIGURE 31. Turbulent-kinetic-energy balance for $R = 0.5$ at $z/D = 0$ and $x/D = 6$; symbols as in figure 29(*a*).

other terms, the resulting dissipation is not inconsistent with that determined from the spectra, as can be seen from the balance shown in figure 29(*b*). This gives some support to the measured convection distribution. Fairly large error bars have been attached to the curves in the energy balance of figure 29(*b*), and this balance must be considered as tentative. It shows that convective transport of $\overline{q^2}$ plays a very important role at the exit plane but that diffusion by the turbulent motion is apparently of secondary importance. Further, the production near the upstream edge is fairly large, while all terms in the energy balance are fairly small towards the downstream edge (but not too close to it).

Figure 30(*a*) shows the individual production terms along a vertical line at $x/D = 4$. The flow behaves now more like a regular shear layer, containing a mixing-layer region with sizeable velocity gradient and underneath it a wake-type region with little variation in the velocity. In the mixing-layer region, the shear-stress production is much larger than the normal-stress production, while in the wake-type region all production terms are of the same order of magnitude but they are all much smaller than the shear production in the mixing-layer region. The energy balance at this x-location is shown in figure 30(*b*) and looks much like the energy balances measured in plane mixing layers (for a review see Rodi 1975). It has been found to be typical for mixing layers that the production is the largest term and is about 1.5 times the dissipation, that both convection and diffusion are quite important, especially near the freestream edge, where they extend considerably beyond the region where production and dissipation are significant and where they balance each other. In this region $\overline{q^2}$ diffuses outward while fluid is entrained (convection) from the freestream, which carries little turbulence. At the inner edge, similar processes take place, but the magnitude of the terms is much smaller. As has already been mentioned, production is rather small in the wake-type region, but it is clear that $\overline{q^2}$ is transported into this region by diffusion, which makes the $\overline{q^2}$ profile more uniform (see figure 19*a*). ϵ determined from the spectra of u is quite similar to that found from the difference of the other terms, which indicates that the pressure diffusion is not very important in this case, a conclusion reached for mixing layers already by Bradshaw, Ferris & Johnson (1964). It should be mentioned here that at this station the terms in the energy balance could be determined with much greater accuracy than at the exit plane.

Figure 31 displays the turbulent-kinetic-energy balance further downstream at $x/D = 6$. It is obvious that all terms have much smaller magnitudes now (they have also been non-dimensionalized with U_e and D). The behaviour in the outer part of the mixing-layer region is rather similar to that observed at $x/D = 4$; that is, the production is larger than the dissipation and at the very edge convection and diffusion balance each other. However, the terms are now more uniformly distributed over the entire height of the flow; that is, there is no clear wake-type region in which the terms are much smaller than in the mixing-layer region. At this station, the inner region gains kinetic energy not only by lateral diffusion from the mixing-layer region but also by convection from upstream regions with higher energy levels. Since convection and diffusion are rather important, turbulence at this station is still far from equilibrium, and it will take some further distance before the mixing-layer and wake regions have disappeared completely and a boundary-layer-type flow remains.

5. Conclusions

The present detailed measurements, supported by the visualization study of Foss (1980), allow the following picture to be drawn of the complex jet-in-a-crossflow situation. At small ratios R of jet-to-crossflow velocity, the jet is bent over abruptly by the crossflow; in the case of $R = 0.5$, for example, this process is nearly complete at the rear of the exit. At higher R-values the jet penetrates further into the cross-stream, and the bending over takes place more gradually. The oncoming crossflow is deflected around the jet and, at low R-values, also lifted over the bent-over jet. A wake region with velocity deficit and relatively small gradients of streamwise velocity develops in the lee of the jet. The extent of this region increases with increasing R. The lower pressure in the wake induces a lateral inward motion and also a downwash of the bent-over jet. Very near the wall, reverse flow occurs. The inward motion transports high-momentum cross-stream fluid to the centreplane, and, in the cases with higher R-values where this effect is stronger, leads to the formation of a wall-jet-type layer with increased velocity. The wake region is displaced from the wall by this layer. For all velocity ratios, a shear layer with significant gradients of the streamwise velocity forms above the wake. In this layer the streamwise velocity varies from the lower values in the wake to the freestream value, with overshoots close to the exit occurring even in the case of the lowest velocity ratio $R = 0.5$. As one proceeds downstream, the wake is 'filled up', and the velocity gradients in the shear-layer and wall-jet regions are diminished; slowly the flow develops towards a boundary layer, with no memory of the jet. Superimposed on the picture portrayed so far is a secondary longitudinal vortex motion which is present also at the lowest velocity ratio $R = 0.5$. This motion, in the form of bound vortices, results from a reorientation and stretching of the original pipe-flow vorticity, but also from shearing at the interface of the originally orthogonal jet and crossflows. The first mechanism is the dominant one at small velocity ratios R and the second at higher R-values. The bound vortex motion is stronger at higher R-values and also persists longer in the downstream direction.

The vortex motion opposes the downwash but strengthens the inward motion caused by the low pressure in the wake. The deflection of the oncoming boundary layer by the jet generates a horseshoe vortex counterrotating to the bound vortex. However, the latter seems to be so much stronger that the former is suppressed, except perhaps at large velocity ratios, where some (but rather weak) evidence was found that the horseshoe vortex was present in the 'hollow' underneath the bound vortex.

At low velocity ratios there is a strong interaction between jet and crossflow in the

exit region. The crossflow acts like a partial cover over the exit, causing a strongly non-uniform exit velocity profile and a sharp bending over of the jet, which starts already inside the discharge pipe. Accordingly, the streamlines are strongly curved, and this curvature acts to stabilize turbulence in the rear part of the exit and to destabilize it in the front part.

The turbulence measurements have shown that the turbulent kinetic energy $\frac{1}{2}q^2$ and the primary shear stress $\overline{uv}$ are closely related to the velocity gradient $\partial U/\partial y$, so that, in general, $\overline{uv}$ can be described by an eddy-viscosity model. However, in certain regions with fairly strong streamline divergence or convergence, the gradient $\partial W/\partial z$ also contributes significantly to the production of q^2 and $\overline{uv}$. For low R-values, the kinetic-energy balance at the exit is rather unusual as production by all velocity gradients is significant and so is convection, in particular by the upward V-velocity; further downstream the energy balance is rather similar to that measured in mixing layers. The shear stress $\overline{uw}$ controlling the lateral spreading of the jet was found to be generated mainly by the two velocity gradients $\partial U/\partial z$ and $\partial W/\partial y$. Since the latter does not appear in the eddy-viscosity relation for $\overline{uw}$, this relation cannot describe $\overline{uw}$ realistically. Rather, a more refined model is necessary which accounts for the production of $\overline{uw}$ by $\partial W/\partial y$. The shear stress $\overline{vw}$, which acts to damp the secondary vortex motion, was found to be related closely to the gradients $\partial V/\partial z$ and $\partial W/\partial y$ and can probably be simulated in general with an eddy-viscosity model.

The research reported in this paper was sponsored by the Deutsche Forschungsgemeinschaft via the Sonderforschungsbereich 80. The authors would like to acknowledge useful discussions with Professor J. F. Foss and the technical assistance of Mr D. Bierwirth. The data evaluation was carried out on the UNIVAC 1108 computer of the University of Karlsruhe.

REFERENCES

ANDREOPOULOS, J. 1980 Digital techniques and computer programs for hot-wire data processing. *Rep.* SFB 80/ME/181, *Univ. Karlsruhe.*

ANDREOPOULOS, J. 1981*a* Using numerical techniques to improve the performance of triple hot-wire probes. In *Proc. 7th Biennial Symp. on Turbulence, Rolla, Mi., USA.*

ANDREOPOULOS, J. 1982 Measurements in jet-pipe flow issuing perpendicularly into a cross stream. *Trans. ASME* I: *J. Fluids Engng.* **104**, 493–499.

ANDREOPOULOS, J. 1983*a* Improvement of the performance of triple hot-wire probes. *Rev. Sci. Instrum.* **54**, 733–740.

ANDREOPOULOS, J. 1983*b* Statistical error analysis associated with probe geometry and turbulence intensity in hot-wire anemometry. *J. Phys.* E: *Sci. Instrum.* (to appear).

ANDREOPOULOS, J. 1983*c* Heat transfer measurements in a heated jet-pipe flow issuing into a cold cross-stream. *Phys. Fluids.* **26**, 3201–3210.

ANDREOPOULOS, J. & WOOD, D. H. 1982 The response of a turbulent boundary layer to a short length of surface roughness. *J. Fluid Mech.* **118**, 143–164.

BERGELES, G., GOSMAN, A. D. & LAUNDER, B. E. 1976 The near-field character of a jet discharged normal to a main stream. *Trans. ASME* C: *J. Heat Transfer* **98**, 373.

BRADSHAW, P. 1973 Effects of streamline curvature on turbulence. *AGARDograph* 169.

BRADSHAW, P., FERRIS, D. H. & JOHNSON, R. F. 1964 Turbulence in the noise-producing region of a circular jet. *J. Fluid Mech.* **19**, 591–624.

CRABB, D., DURÃO, D. F. G. & WHITELAW, J. H. 1981 A round jet normal to a cross flow. *Trans. ASME* I: *J. Fluids Engng* **103**, 142–152.

ERMSHAUS, R. & NAUDASCHER, E. 1977 Der Niedergeschwindigkeitskanal des Instituts für Hydromechanik an der Universität Karlsruhe. *Z. Flugwiss. Weltraumforschung* **1**, 419–425.

Foss, J. 1980 Interaction region phenomena for the jet in a cross-flow problem. *Rep.* SFB 80/E/161, *Univ. Karlsruhe.*

Keffer, J. F. & Baines, W. D. 1963 The round turbulent jet in a cross wind. *J. Fluid Mech.* **15**, 481–496.

Komotani, Y. & Greber, I. 1972 Experiments and turbulent jet in a cross flow. *AIAA J.* **10**, 1425–1429.

McMahon, H. M., Hester, D. D. & Palfery, J. G. 1971 Vortex shedding from a turbulent jet in a cross wind. *J. Fluid Mech.* **48**, 73–80.

Moussa, Z. M., Trischka, J. W. & Eskinazi, S. 1977 The near field in the mixing of a round jet with a cross stream. *J. Fluid Mech.* **80**, 49–80.

Ramsey, J. W. & Goldstein, R. J. 1971 Interaction of a heated jet with a deflecting stream. *Trans. ASME* C: *J. Heat Transfer* **94**, 365–372.

Rodi, W. 1975 A review of experimental data of uniform-density free turbulent boundary layers. In *Studies in Convection* (ed. B. Launder), vol. 1, pp. 79–166. Academic.

Townsend, A. A. 1976 *The Structure of Turbulent Shear Flow*, 2nd edn. Cambridge University Press.

Yavuzkurt, R. J., Moffat, R. J. & Kays, W. M. 1977 Full-coverage film cooling: 3-dimensional measurements of turbulence structure and prediction of recovery region hydrodynamics. *Rep.* HMT-27, *Stanford Univ.*